CONTENTS

PUBLICATION POLICY

The *ECMWF Newsletter* is published quarterly. Its purpose is to make users of ECMWF products, collaborators with ECMWF and the wider meteorological community aware of new developments at ECMWF and the use that can be made of ECMWF products. Most articles are prepared by staff at ECMWF, but articles are also welcome from people working elsewhere, especially those from Member States and Co-operating States. The *ECMWF Newsletter* is not peer-reviewed.

Editor: Bob Riddaway

Typesetting and Graphics: Rob Hine

Any queries about the content or distribution of the *ECMWF Newsletter* should be sent to Bob.Riddaway@ecmwf.int

Guidance about submitting an article is available at www.ecmwf.int/publications/newsletter/guidance.pdf

CONTACTING ECMWF

Shinfield Park, Reading, Berkshire RG2 9AX, UK

Fax:		+44 118 986 9450
Telephone:	**National**	0118 949 9000
	International	+44 118 949 9000
ECMWF website		www.ecmwf.int

All change!

They say that it's hard to cope with change in life but as meteorologists we thrive on the changeability of the weather – where would weather forecasting be without it!

At ECMWF in July we will be introducing two new Departments replacing our existing Operations Department – the Forecast and Computing Departments.

- The Forecast Department comprises a strong user-focus, with meteorological input to forecast production, forecast evaluation and diagnostics, forecast products and applications, software development, and catalogue and data services.
- The Computing Department comprises the 24/7 operation of the computing infrastructure and forecast production at ECMWF.

The organisational structure of ECMWF reflects the critical outputs for the organisation which can be expressed in terms of four foci:

- NWP and connected research
- 24/7 operations
- forecasts, products and data for users
- administrative support

Having a department for each focus provides clear missions for each department and the ability to more flexibly allocate resources and solve problems that arise.

One of the key activities for ECMWF (and this will be led by the Forecast Department) is evaluation of our forecast skill. This is not easy although it is one of the beauties of meteorological science that we can be objective and quantitative about the accuracy of our predictions. Difficulties arise in the most mundane places.

These days one frequently sees headlines in the media about the weather becoming less predictable. Of course to a specialist in numerical weather prediction this feels like a misuse of the word predictable. What does the journalist mean by it? It could be that the weather seems more changeable – first a drought then a flood then a windstorm in quick succession. But to a specialist such a sequence of weather may be both changeable and extremely well predicted. Another interpretation of less predictable is that the weather doesn't seem like it used to be "when I was a child". This in effect evaluates the current weather sequence relative to a purely climatological prediction. Meteorologists set the bar high on their forecasts – they have to beat a climatological prediction to be skilful. A further interpretation is that the weather has changed rapidly compared to yesterday's or last week's weather. This is another form of prediction – based on persistence – and again meteorologists' forecasts have to beat persistence.

Another important aspect in the evaluation of forecasts is how to evaluate an ensemble or probabilistic forecast. Can an individual probabilistic forecast ever be wrong if it, as it must, uses probabilities other than 0% or 100%? ECMWF places great store by both the accuracy and reliability of its forecasts so that when a probability of 30% is predicted then indeed that is the frequency with which that event actually occurs when given that probability. But for the media and the public it can feel underwhelming if a forecaster has predicted a 10% chance of rain and there is heavy rain all day – even if we earnestly say that this was a trustworthy ensemble forecast! Let's wish the new Forecast Department every success in its evaluation of the skill of our forecasts.

Alan Thorpe

New items on the ECMWF website

ANDY BRADY

Use of GIS/OGC standards in meteorology

The '*4th Workshop on the Use of GIS/OGC Standards in Meteorology*' was held from 4 to 6 March 2013. The aim of this workshop was to provide a new roadmap for the MetOcean DWG with a focus on standards that have not so far been covered by various working groups and any other standards that may be relevant for the meteorological community. Presentations and outcomes are available. See the news item on page 5 for more information.

- http://www.ecmwf.int/newsevents/meetings/workshops/2013/GIS-OGC_standards/

Workshop on 'Parameter estimation and inverse modelling for atmospheric composition'

This will be held at ECMWF from 22 to 24 October 2013. The aim of the workshop is to explore the options to optimally define the boundary conditions in a near-real-time 4DVAR data assimilation system.

- http://www.ecmwf.int/newsevents/meetings/workshops/2013/Parameter_estimation/

Using ECMWF's forecasts (UEF2013)

A forum to discuss the use and performance of ECMWF's forecasts and related products will be held from 5 to 7 June 2013. The theme of this year's meeting, which focuses on the applications and impact of weather information, is '*Integrated use of ECMWF forecast products in decision making and risk management*'.

- http://www.ecmwf.int/newsevents/meetings/forecast_products_user/

Ocean reanalyses intercomparison

The next '*CLIVAR GSOP/GODAE Ocean View Workshop on Ocean Reanalyses Intercomparison*' will be held at ECMWF from the 1 to 3 July 2013. Several ocean reanalyses products are produced worldwide with different purposes and methodologies. The intercomparison exercise aims at understanding the consistency and differences in the products under different metrics, evaluation of fit-for-purpose products, and exploitation of this variety of reanalysis using the ensemble approach to target different areas. The workshop attendance is by invitation only.

- http://www.ecmwf.int/newsevents/meetings/workshops/2013/CLIVAR/

ECMWF 2013 Annual Seminar

The 2013 Annual Seminar will cover recent developments in numerical methods for atmosphere and ocean modelling; it will be held from 2 to 5 September. The seminar will present a pedagogical review of recent advances and future challenges in high-resolution numerical modelling. Topics to be covered will include a discussion of various approximations to the fully-compressible Euler equations, different horizontal and vertical discretizations and time-integration schemes, as well as questions of stability, accuracy and conservation. Issues of efficiency on the massively parallel computer architectures of the future will also be addressed.

- http://www.ecmwf.int/newsevents/meetings/annual_seminar/2013/

New Public Data Server

ECMWF is deploying an updated public data server service and the new system is already available in parallel with the existing one. Data from DEMETER, Reanalysis (ERA), GEMS, MACC, TIGGE and YOTC are all available. An experimental release of ERA-Interim data batch access is also available.

- http://data.ecmwf.int/data/

Webinars: what are they?

ANNA GHELLI

During recent training courses on '*Use and interpretation of ECMWF products*' we introduced webinars to provide distance training to forecasters. Webinars (seminars on the web) are a well-established tool for one-to-many communications through the internet. They combine audio and visual components, which are important elements in the learning process. Moreover, lecturer and attendees do not have to be physically in the same room, saving travel time and money. Webinars offer an interactive medium which is ideal for tutorials with live question and answer sessions.

We have offered a number of events since October 2012 including those dealing with applications of seasonal forecasts to droughts and malaria warning systems, introduction to monthly forecasting, and ECMWF products for extreme weather events.

The sessions were very popular with more than a hundred participants for the topical lectures on monthly forecasting and extreme weather products.

Forecasters from National Meteorological Services in both Member and Cooperating States participated in the webinars thanks to the support of ECMWF meteorological contact points who advertised the events in their own Services.

Initially this remote training activity was developed in conjunction with the training course on the use and interpretation of ECMWF products. However having realised the potential of webinars, it was decided to extend them to Metview training and other introductory sessions on specific NWP topics. The first Metview webinar was run in March 2013 attracting more than one hundred participants from Europe and Africa, as Metview is distributed as open source code.

In April 2013 we ran an introductory webinar on surface processes and in June 2013 there will be two sessions on data assimilation for screening parameters with particular focus on snow assimilation.

If you or any of your colleagues are interested in future webinars, please visit

- https://ecmwf.webex.com/mw0307l/mywebex/default.do?siteurl=ecmwf

Routine verification of radiation and cloudiness

THOMAS HAIDEN

Accurate prediction of cloudiness is crucial in weather forecasting. Throughout the troposphere, clouds exert a strong feedback on atmospheric flow by modulating energy fluxes and heating rates. Errors in low cloudiness contribute significantly to 2-metre temperature errors in the short and medium range from HRES. In the past, routine verification of cloudiness at ECMWF was mainly based on SYNOP observations. Recently this has been extended to include satellite-derived products and data from a network of surface radiation stations.

The EUMETSAT Climate Monitoring Satellite Application Facility (CM-SAF) provides various cloud and radiation products for the area covered by the Meteosat Second Generation (MSG) satellite. The first figure shows verification results for the three-day forecasts of 24-hour means of downward solar radiation at the surface for 2012. Monthly values of temporal correlation are used as a metric, which is insensitive to any biases in the datasets. Fluxes have been scaled by their clear-sky values, allowing direct comparison across latitudes and aggregation over seasons. The results highlight regional differences of skill in predicting day-to-day changes of solar radiation reaching the Earth's surface. In most regions such changes are primarily due to variations in cloudiness.

There is a general decrease of skill from the mid-latitudes towards the tropics. Skill also decreases southward of 50°S, which is an area of high variability in cloudiness due to cyclonic activity. The ECMWF model is known to underestimate low-level cloudiness in this region. In the North Atlantic the poleward decrease of skill starts at a higher latitude and is less pronounced. This hemispheric asymmetry is not completely understood but appears to be related to the less rotationally symmetric land-sea distribution in the north, and a lower frequency of cold-air outbreaks producing the kind of low cloudiness which is underestimated in the forecast.

For a given latitude, correlations tend to be lower over the ocean. This is particularly apparent near the south-west coast of Africa, where marine stratocumulus poses a specific forecasting challenge. Highest skill is reached in Europe, in particular over land areas adjacent to the Mediterranean Sea, and over the extra-tropical southern continents. Lowest forecast skill is found in the southern tropical Atlantic between 0° and 15°S, just south of the main area of deep convection associated with the Inter-tropical Convergence Zone. Here, much of the day-to-day variability is caused by transitions between cloud regimes such as stratocumulus and cumulus.

For verification of absolute radiation values and diagnosis of systematic errors, data from the Baseline Surface Radiation Network (BSRN) is used. It comprises more than 50 stations which provide high-quality surface radiation flux measurements for monitoring climate change as part of the World Climate Research Programme (WCRP). A subset of this data is available sufficiently close to real time to be used in routine forecast verification and model cycle evaluation.

The second figure shows the evolution of the bias and error standard

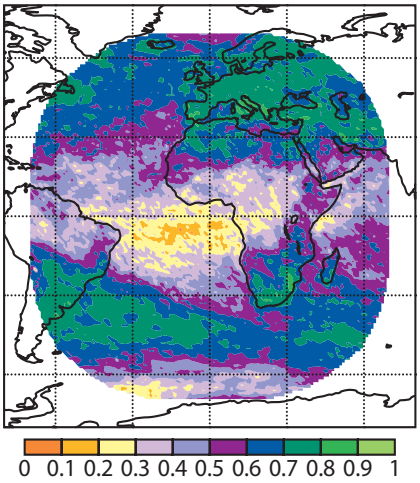

Verification of HRES daily totals of the downward solar flux at the surface. Shown is the temporal correlation of three-day forecasts and observations over monthly periods, averaged over the year 2012. There are large regional differences in the skill of predicting day-to-day changes of solar radiation reaching the Earth's surface. In most regions such changes are primarily due to variations in cloudiness.

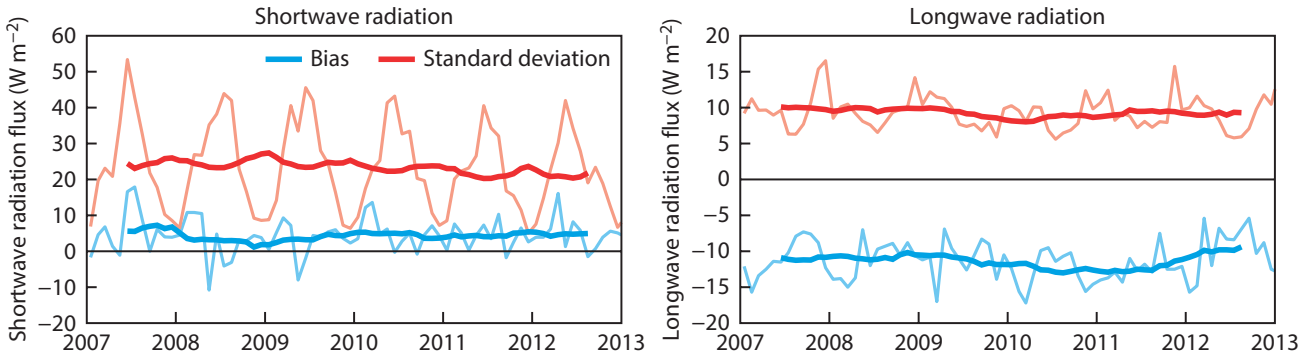

Verification of HRES downward shortwave and longwave radiation. Shown are the bias and standard deviation (SDEV) of the one-day forecasts of shortwave (left) and longwave (right) downward radiation at Cabauw, The Netherlands, based on verification against BSRN data. Both the monthly means and annual (12-month running) means are shown for the bias and SDEV. For the annual means of the shortwave radiation, the bias is rather constant but there is a slight decreasing trend in SDEV. For the longwave radiation both the bias and SDEV show little trend.

deviation (SDEV) of one-day forecasts of downward shortwave and longwave radiation at Cabauw, The Netherlands, over the last six years. Although variations in SDEV of the shortwave flux (upper panel) are dominated by the annual cycle of insolation, a slight trend of decreasing SDEV is noticeable in the annual means. The shortwave bias has remained rather constant at a small value of 5 W m^{-2}. For the longwave flux (lower panel), which at this location has its maximum in winter due to increased cloudiness, the SDEV shows little trend. The negative bias on the order of 10 W m^{-2}, which is found at most BSRN stations, has been a long-standing issue in both NWP and climate models. It appears to be partly due to an underestimation of the liquid water path in low clouds.

Diagnostics such as these will improve the routine monitoring of operational and pre-operational model configurations and provide additional feedback to model developers.

Flow dependent background error modelling in 4DVAR

MASSIMO BONAVITA

Atmospheric data assimilation schemes like 4DVAR try to optimally combine information from a short-range forecast (the background) with new observations. The background essentially contains the information from all previous observations which is then propagated and evolved by the forecast model up to the analysis time. To a large extent, the skill of an assimilation system is determined by the accuracy of the statistical description of errors in the background and the observations. This is because the weight given in the analysis update to the observations depends on the ratio of background error and observation error variances. In addition, the spatial structures of background errors and correlations determine how new information from the latest batch of observations is propagated to data sparse regions.

Since background errors are highly spatially and temporally variable, especially in the proximity of active weather systems, a long-standing objective of research at ECMWF has been to provide realistic, flow-dependent estimates of background errors to the 4DVAR analysis. This goal had been partially achieved in cycles 37r2 and 38r1 of the Integrated Forecasting System (IFS) with the use of error estimates from the ECMWF Ensemble of Data Assimilations (EDA; *Isaksen et al., ECMWF Newsletter No. 123*; *Bonavita et al., ECMWF Newsletter No. 129*). However, a major limitation of those implementations resided in the fact that only the balanced part of the 4DVAR errors (i.e., those errors which are in an approximate geostrophic balance) was estimated online from the EDA. The unbalanced part of the background errors was modelled by spatially homogeneous, static climatological estimates. This inconsistency has been removed in Cy38r2, where

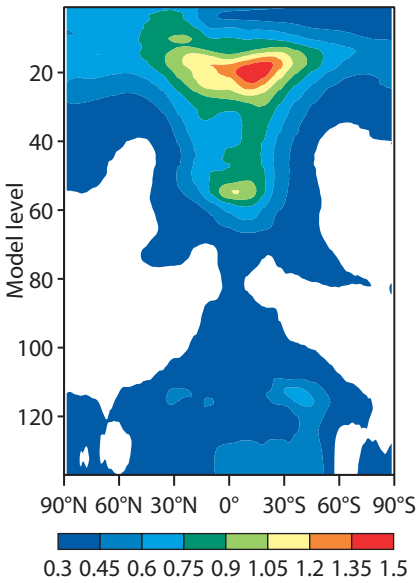

Unbalanced temperature errors estimated from the EDA. Shown is the longitudinal average of unbalanced temperature errors in degrees K estimated from the EDA as a function of model level. Values are averaged over March 2012. Note that the largest impact occurs in the boundary layer and tropical stratosphere.

online estimates of unbalanced errors from the EDA are also used.

An example of the average structure of the unbalanced temperature errors estimated from the EDA is shown in the figure. The largest impact is visible in the boundary layer and in the tropical stratosphere. This is consistent with the expected weakening of the mass-wind balance constraint in the boundary layer and the signature of convection-generated gravity waves in the tropical stratosphere. The introduction of unbalanced errors from the EDA has produced a clear positive impact on the skill of the high-resolution forecast and has contributed to making Cy38r2 a successful upgrade of the IFS.

The change described here is a further step towards a hybrid data assimilation system. Such a system will use a fully flow-dependent representation of background error covariance and this will make it possible to replace the current static covariance by ones updated in real time. This upgrade is currently being tested in pre-operational mode with the goal of implementing it in Cy39r1.

Use of GIS/OGC standards in meteorology

STEPHAN SIEMEN, BAUDOUIN RAOULT

Following the success of the previous workshops, ECMWF, the UK Met Office, Météo-France and Deutscher Wetterdienst (DWD) jointly organised a 4th workshop on the use of GIS/OGC standards in meteorology. This was held at ECMWF from 4 to 6 March 2013.

The Open Geospatial Consortium (OGC) is very active in developing standards that cater for emerging technologies and allow interoperability between communities that previously were not able to easily communicate. Embracing these standards will allow the meteorological community to reach out to a wider audience, and keep up with the ever-changing landscape of Internet-based services.

The main outcome of the first of these workshops (held at ECMWF in 2008) was the establishment in 2009 of a Memorandum of Understanding between the World Meteorological Organization (WMO) and the OGC, and the creation of the OGC MetOcean Domain Working Group (DWG). In 2010 and 2011, alignment of WMO, OGC and aviation conceptual modelling activities took place. Recently, the MetOcean DWG issued a 'best practice' document for the use of Web Map Services (WMS) in meteorology, encompassing the handling of the time and elevation dimensions in requests for meteorological maps.

Participants at the 4th workshop on the use of GIS/OGC standards in meteorology. The workshop was attended by 51 participants from 36 institutions in 17 countries worldwide.

The aim of this 4th workshop was to provide a new roadmap for the MetOcean DWG with a focus on standards that have not yet been covered by the working groups, such as Web Coverage Services (WCS), Sensor Observation Service (SOS), Sensor Web Enablement (SWE), Web Processing Service (WPS) and any other standards that may be relevant for the meteorological community. Speakers shared their plans and/or experiences in implementing OGC standards in their organisation.

Much time was dedicated to discussion and working groups. Two working groups covered experiences, plans and best practices associated with:

- Implementation of INSPIRE.
- Implementation of WCS MetOcean.

The discussion concluded that a MetOcean extension to the WCS should be the highest priority for the coming year and this extension should also meet the requirements set by INSPIRE. Therefore, as next step, it was agreed to establish a working group within the MetOcean DWG to work on WCS.

The activities of this working group will be documented on the MetOcean Wiki page at:

- http://external.opengeospatial.org/twiki_public/MetOceanDWG

The meetings presentations and conclusions for the discussions can be found at:

- http://www.ecmwf.int/newsevents/meetings/workshops/2013/GIS-OGC_standards/

Closer together: coupling the wave and ocean models

ØYVIND BREIVIK, MAGDALENA ALONSO-BALMASEDA, JEAN-RAYMOND BIDLOT, PETER A E M JANSSEN, SARAH KEELEY, KRISTIAN MOGENSEN

Traditionally, wind-generated surface waves have been treated as a phenomenon somewhat detached from the goings-on of the ocean beneath. That waves affect the marine boundary layer of the atmosphere by modifying the surface roughness has long been known. Consequently, since 1998 ECMWF has been running a coupled forecasting system where the atmospheric component of the Integrated Forecasting System (IFS) communicates with the wave model (WAM) through exchange of the Charnock parameter which determines the roughness of the sea surface (*Janssen*, 2004).

If the wave model is allowed to interact with the atmospheric component, it may be pertinent to ask if it should also be allowed to 'talk' to the ocean model, NEMO. This is the topic of the European Union FP7 project MyWave which started in 2012 and runs until the end of 2014.

Waves affect the upper part of the ocean through three distinct mechanisms which are illustrated in Figure 1.

- ***Stress***. When waves are growing they soak up momentum (and thus energy) which otherwise would have been transferred to the ocean interior. This is shown in the left part of Figure 1 as the difference τ_w between the air-side stress on the water surface (τ_a) and the water-side stress (τ_o).
- ***Turbulent kinetic energy.*** As waves break (right side of Figure 1) they inject turbulent kinetic energy, thus enhancing the mixing, while also feeding momentum into the currents. If there is equilibrium between wind input and dissipation, then the airside stress would be equal to the total water-side stress. However, most of the time waves are not in equilibrium giving differences in air-side and water-side stress of the order of 5–10%, which is not an inconsiderable difference.
- ***Stokes drift.*** Waves set up a current in the down-wave direction known as the Stokes drift. Although this effect decays rapidly with depth, it can be substantial near the surface (~1 m/s). In combination with the earth's rotation it adds an additional veering to the upper-ocean currents known as the Coriolis-Stokes force (see e.g. *Janssen*, 2012; *Belcher et al.*, 2012).

All three of the above mechanisms are already available from WAM, both as operational forecast products (since June 2012) and in the ERA-Interim reanalysis (1979 to present, see *Dee et al.*, 2011).

To test the impact of wave information on the upper ocean we have performed experiments where wave effects are introduced in NEMO. A comparison was made between stand-alone (ocean only) integrations where (a) stress, energy flux and Stokes drift are taken from the ERA-Interim archive and (b) a control run without Stokes drift and with an energy flux based on fully developed wind sea. Therefore, the control run also includes the effect of breaking waves on upper-ocean mixing, but ignores the effect of growing and decaying wind sea on the energy and momentum fluxes (*Craig & Banner*, 1994). The integration covered the thirty-one years from 1979 to 2009.

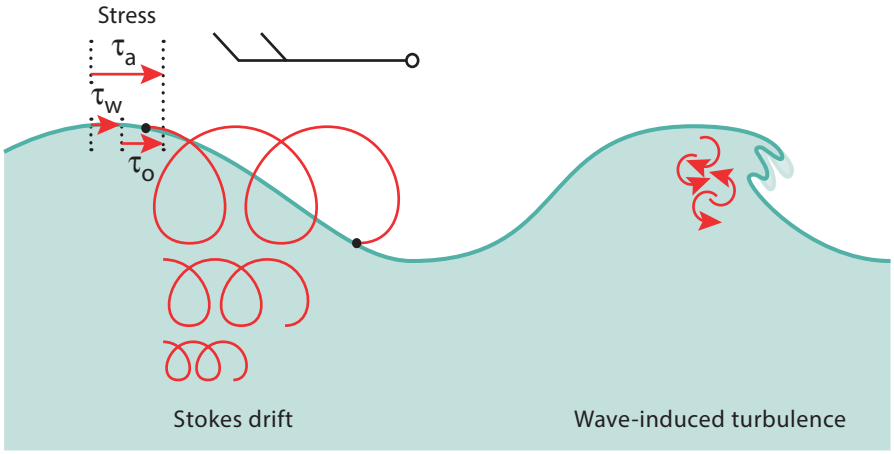

Figure 1 Wave-ocean interaction. As waves grow under the influence of the wind (left), the waves will absorb momentum (τw) which otherwise would have gone into the ocean directly (τo). As waves break (right), turbulent kinetic energy is injected into the ocean mixed layer, significantly enhancing the mixing. The Stokes drift, a Lagrangian effect of waves of finite amplitude, sets up a current in the along-wave direction which decays rapidly with depth. Near the surface it may become substantial (~1 m/s). The Coriolis effect works on the Stokes drift and adds a new term to the momentum equations known as the Coriolis-Stokes force.

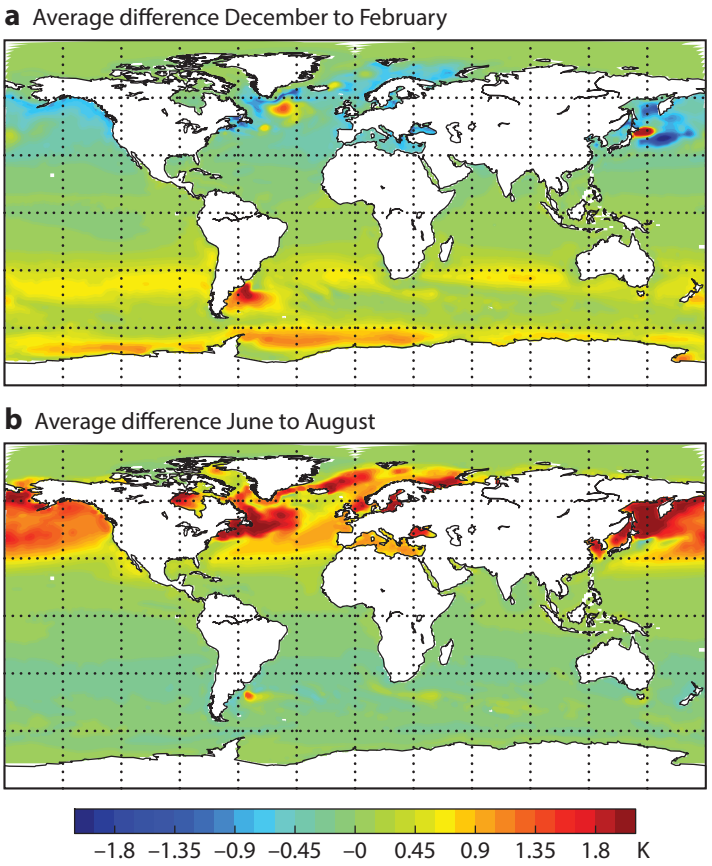

Figure 2 Temperature difference between a control run with energy flux estimated from an average sea state and a run where wave effects are computed from the ERA-Interim WAM model (averaged over the period 1989–2008) for (a) December to February and (b) June to August. The effects are most pronounced in the extratropics of the summer hemisphere, where the difference amounts to more than 2 K. The effect of the Coriolis-Stokes force and the modified momentum flux is most pronounced in the Gulf Stream and Kuroshio currents.

The sea surface temperature differences are shown in Figure 2. The sea-state dependent mixing gives rise to rather large temperature differences with the biggest deviations found in the summer hemisphere. This is partly due to too vigorous mixing in the control run. Whereas the temperature differences due to modified mixing are quite uniform throughout the extratropics, the differences linked to the Coriolis-Stokes effect are more localized. The pronounced differences found in the Kuroshio and Gulf Stream stem from both Coriolis-Stokes forcing and modifications to the stress. Overall the differences amount to more than 2 K in the extratropics.

In the experiments shown in Figure 2, NEMO is updated with wave fields four times daily. However, in the new coupled model system (see *Mogensen et al.*, 2012) which is now under development, WAM, NEMO and the atmospheric model are tightly integrated. It is expected that this system will allow efficient exchange of a large number of fields at high temporal frequency. Early results with fully coupled runs indicate an impact from the coupling of WAM and NEMO also on the atmosphere. But, no matter how large the wave effects in the end will turn out to be, the tight coupling under development opens up new possibilities for exchange of parameters, not just between the wave model and the ocean model, but also the other way round.

FURTHER READING

Belcher, **S.E.**, **A.L.M. Grant**, **K.E. Hanley**, **B. Fox-Kemper**, **L. Van Roekel**, **P.P. Sullivan**, **W.G. Large**, **A. Brown**, **A. Hines**, **D. Calvert**, **A. Rutgersson**, **H. Pettersson**, **J.-R. Bidlot**, **P.A.E.M. Janssen** & **J.A. Polton**, 2012: A global perspective on Langmuir turbulence in the ocean surface boundary layer. *Geophys. Res. Lett.*, **39**, L18605, doi:10.1029/2012GL052932.

Craig, **P.D.** & **M.L. Banner**, 1994: Modeling wave-enhanced turbulence in the ocean surface layer. *J. Phys. Oceanogr.*, **24**, 2546–2559, doi:10/df29g2.

Dee, **D.**, **S. Uppala**, **A. Simmons**, **P. Berrisford**, **P. Poli**, **S. Kobayashi**, **U. Andrae**, **M. Balmaseda**, **G. Balsamo**, **P. Bauer**, **A. Beljaars**, **L. van de Berg**, **J. Bidlot**, **N. Bormann**, ***et al.***, 2011: The ERA-Interim reanalysis: Configuration and performance of the data assimilation system. *Q. J. R. Meteorol. Soc.*, **137**, 553–597, doi:10.1002/qj.828.

Janssen, **P.**, 2004: The Interaction of Ocean Waves and Wind. *Cambridge University Press*, Cambridge, UK, 233–244.

Janssen, **P.**, 2012. Ocean wave effects on the daily cycle in SST. *J. Geophys. Res.*, **117**, C00J32, 24 pp, doi:10.1029/2012JC007943.

Mogensen, **K.**, **S. Keeley** & **P. Towers**, 2012: Coupling of the NEMO and IFS models in a single executable. *ECMWF Tech. Memo No. 673.*

The new MACC-II CO_2 forecast

ANNA AGUSTÍ-PANAREDA, SEBASTIEN MASSART, SOUHAIL BOUSSETTA, GIANPAOLO BALSAMO, ANTON BELJAARS, FRÉDÉRIC CHEVALLIER, RICHARD ENGELEN, VINCENT-HENRI PEUCH, MIHA RAZINGER

A new global atmospheric forecast of CO_2 is available as part of the pre-operational Monitoring of Atmospheric Composition and Climate – Interim Implementation (MACC-II) project. MACC II is funded by the European Community's Seventh Framework Programme and uses the infrastructure of ECMWF's Integrated Forecasting System (IFS). Monitoring and understanding the current CO_2 variability is a prerequisite for climate projection and climate change adaption, since it is the most abundant greenhouse gas with a large human-induced contribution. In this article we present one of the first operational CO_2 forecast products that is available in real time. This is important because it opens up the possibility of assimilating CO_2 observations in the IFS. It also allows the full interaction of the modelling of vegetation (via biogenic CO_2 fluxes), water cycle (via evapotranspiration) and radiation (via atmospheric CO_2) within the ECMWF modelling framework.

First, we discuss the causes of CO_2 variability and describe the configuration of the forecast. Then we show the capability of the forecast to simulate CO_2 variability on different spatial and temporal scales by comparing forecasts with observations. The main sources of forecast error are pointed out as well as planned future work to address those issues. Finally, information on how to access the near-real-time CO_2 plots and the monitoring of the forecast, as well as the forecast data, is provided for anybody interested in using the CO_2 forecast product. Some of the potential applications of the CO_2 forecast are listed in Box A.

CO_2 variability

The variability of atmospheric CO_2 concentration results from variations in surface fluxes and atmospheric transport, which are coupled. The challenge of forecasting CO_2 globally arises from the large uncertainties in the simulation of the CO_2 sources and sinks and of atmospheric transport (particularly within the atmospheric boundary layer).

Globally, CO_2 variability on time scales ranging from diurnal, through seasonal to inter-annual is dominated by variations in the vegetation fluxes over land. The photosynthesis in plants and the respiration in both plants and organic soils result in large amounts of CO_2 being removed from and released into the atmosphere. These two processes vary with temperature, availability of moisture and radiation; hence producing daily, seasonal, annual and latitudinal variations in atmospheric CO_2 concentrations.

The recent development of the CTESSEL simplified land carbon module (*Boussetta et al.*, 2013) used in the IFS provides terrestrial biogenic CO_2 fluxes in real time with accurate real-time meteorological forcing. It also ensures consistency between meteorological forcing of CO_2 biogenic fluxes and CO_2 transport.

An example of the importance of this consistency between forcing and transport is the passage of mid-latitude frontal weather systems. The change in radiation associated with the frontal clouds reduces photosynthetic CO_2 uptake which results in a substantial increase in atmospheric CO_2, of the order of 10 ppm. This CO_2 concentration anomaly is then transported by frontal ascent to the mid- and upper-troposphere.

The coupling between fluxes and transport also works on seasonal scales. Namely, meridional transport by mid-latitude weather systems reduces/amplifies the CO_2 seasonal cycle at mid/high latitudes (*Parazoo et al.*, 2011). On both diurnal and seasonal time scales, there is also a strong coupling between turbulent mixing near the ground and terrestrial biogenic fluxes, known as the rectifier effect (*Denning et al.*, 1999).

Forecast configuration

The CO_2 surface fluxes representing the various CO_2 sources and sinks in the CO_2 forecast are described in Box B. At present, the CO_2 forecast runs daily in a cyclic mode. That is, the atmospheric CO_2 is initialized each day at 00 UTC with the previous 24-hour forecast; this is in contrasts with the NWP framework, where initial conditions are constrained by observations. In order to avoid growing CO_2 biases, the atmospheric CO_2 field is re-initialized on 1 January from simulations with the latest available opti-

Applications for the CO_2 forecast — A

The target applications of the MACC-II global CO_2 product include:

- Providing boundary conditions for regional modelling and flux inversions.
- Improving the modelling of the radiative tranfer and evapotranspiration in Numerical Weather Prediction (NWP) analysis and forecast.
- Evaluation of transport processes in the IFS (e.g. diffusion, convection and advection).
- Providing prior information for CO_2 and CH_4 satellite retrievals.
- Supporting the interpretation and quality control of observations via monitoring activities.
- Supporting the planning of field experiments.

CO_2 surface fluxes

B

The following outlines the CO_2 surface fluxes that represent the various CO_2 sources and sinks in the CO_2 forecast.

- CTESSEL includes a light-efficiency photosynthesis model driven by radiation, soil moisture and soil temperature. It has a simple parametrization for respiration driven by soil moisture, soil temperature and snow cover. The vegetation growth is derived from a MODIS-based LAI climatology and land use change is not represented. There is no direct simulation of the different carbon pools, but a reference respiration parameter for each vegetation type is used to simulate the ecosystem respiration. The reference value is obtained by optimization with respect to flux measurements for the different vegetation types. A detailed description and evaluation of the CTESSEL biogenic fluxes has been provided by (*Boussetta et al.*, 2013, *ECMWF Tech. Memo. No. 675*).
- The near-real-time fire flux is from GFAS v1.0 *Kaiser et al.*, 2012, *Biogeosciences*, **9**, 527–554)
  - http://www.gmes-atmosphere.eu/about/project_structure/input_data/d_fire/

  a daily temporal resolution and a horizontal resolution of 0.5° ×0.5°. The fire fluxes are kept constant throughout the 5-day forecast.
- The ocean sink is from the *Takahashi et al.* (2009, *Deep-Sea Res. II*, **56**, 554–577) climatology with monthly mean fluxes at 4° x 5° resolution.
- The anthropogenic fluxes are annual mean fluxes based on the last year (2008) of the EDGAR version 4.2 inventory
  - http://edgar.jrc.ec.europa.eu

  in order to account for the increase in the emissions since 2008, the growth in anthropogenic emissions beyond 2008 has been represented using a global rescaling factor based on estimated and climatological anthropogenic CO_2 emission trends.

mized fluxes provided by the MACC-II flux inversion system at Laboratoire des Sciences du Climat et l'Environnement (LSCE, *Chevallier et al.*, 2011). The meteorological fields are initialized with ECMWF operational analyses each forecast cycle.

The resolution of the CO_2 forecast is the same as the operational weather forecast. Currently, it has a lead time of 5 days with fields archived every 3 hours. This can be easily extended to longer lead times for specific user requirements.

Annual global budget

The increase of atmospheric CO_2 concentration in the model is the result of the addition of all the CO2 surface fluxes shown in Figure 1. Because the CO_2 fluxes in the model are not constrained by observations, the sum of the total emissions (i.e. the budget) does not match the observed atmospheric increase. This leads to an annual global bias in the forecast of CO_2. This bias and the modelled atmospheric concentration increase are both modulated by the inter-annual variability of the terrestrial biogenic fluxes. The correlation between the forecast and observed global annual atmospheric growth is 0.74. Although the main contributor to the CO_2 sink associated with the terrestrial biogenic fluxes is the northern hemisphere, the tropics are responsible for its large inter-annual variability.

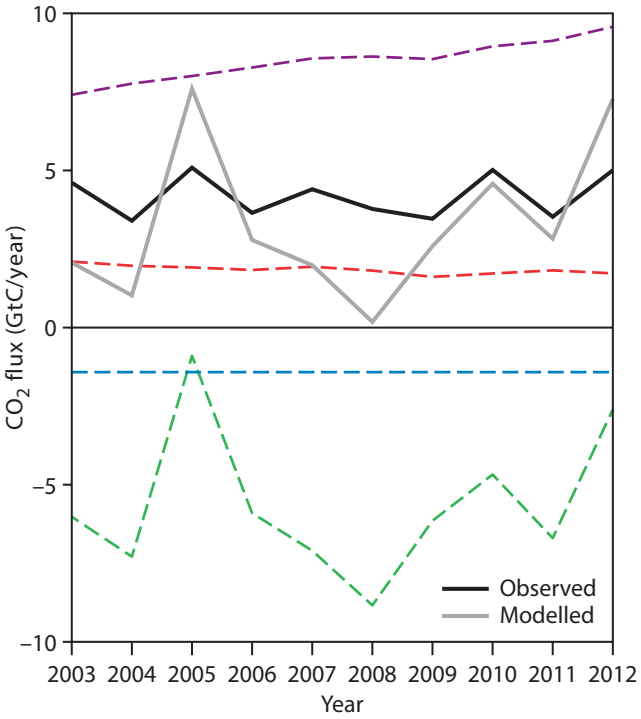

Figure 1 Annual global budget for the modelled total CO_2 flux (grey) compared to the observed CO_2 atmospheric growth from NOAA (http://www.esrl.noaa.gov/gmd/ccgg/trends/) (black) from 2003 to 2012. The different flux components are shown by the other coloured lines: anthropogenic (purple), fires (red), ocean (blue) and land vegetation (green). The units are gigatons of carbon (GtC).

Seasonal cycle

The phase and amplitude of the CO_2 seasonal cycle vary with latitude. The model is evaluated using the NOAA GLOBALVIEW-CO2 (2011) dataset which provides the integrated effects of surface CO_2 fluxes over large regions at different latitudinal bands.

At first glance, the seasonal cycle phase and amplitude and latitude dependence shown in Figure 2 appear to be reasonably well represented in the forecast. However, there are clear discrepancies between the forecast and GLOBALVIEW-CO2 product in the northern hemisphere.

- In the forecast not enough CO_2 is released before and after the growing season (i.e. March to May and October to December).
- The onset of the CO_2 sink associated with the growing season starts too early in the forecast (e.g. the sharp CO_2 decrease in mid-latitudes depicted by GLOBALVIEW-CO2

product in June starts in May in the forecast). This also leads to a longer growing season in the forecast.

The combination of these two factors is consistent with the predominantly negative global annual bias shown in Figure 1.

Synoptic variability

The passage of frontal low pressure systems is responsible for the long-range transport of CO_2 via their warm conveyor belts which lift CO_2-rich air from the surface to the mid- and upper-troposphere. This large-scale advection is illustrated in Figure 3a where positive CO_2 anomalies originating from the surface are shown in the region of frontal ascent within a low pressure system at various vertical levels (850, 500 and 300 hPa).

The synoptic variability of CO_2 associated with the passage of low pressure systems is well captured by the forecast at the NOAA/ESRL tall tower in Park Falls (Winsconsin, USA), as shown in Figures 3b and 3c throughout September. The high peaks of CO_2 concentration can originate from the advection of CO_2-rich anomalies, as well as the synoptic variability of the CO_2 net ecosystem exchange fluxes.

The cloudy warm conveyor belts in the mid-latitude low pressure systems are associated with changes in temperature and solar radiation at the surface which in turn produce an increase in the net ecosystem exchange. As shown in Figure 4, this increase can be linked with the following.

- A decrease in the photosynthetic uptake following a decrease in radiation (e.g. 3 and 7 September) – see panels 4a and 4c.
- An increase in ecosystem respiration following an increase in temperature (e.g. 21 September) – see panels 4a and 4b.
- Both, a simultaneous decrease in the vegetation uptake and increase in ecosystem respiration due to a concurrent decrease in radiation and increase in temperature (e.g. 11 and 23 to 24 September) – see panels 4a, 4b and 4c.

The landfall of hurricane Sandy in 2012 provides another example of the importance of the passage of low-pressure systems in the modulation of CO_2 synoptic variability and long-range transport. The various CO_2 anomalies shown in Figure 5 are associated with convective, synoptic and large-scale transport mechanisms. Thus, the CO_2 forecast opens the possibility of using CO_2 as a tracer to provide information about the transport processes in NWP models.

Diurnal cycle

Over vegetated areas, CO_2 concentration is characterized by a strong diurnal cycle controlled by the CO_2 biogenic fluxes – daytime uptake and night time release – as well as the boundary layer increased/decreased mixing during daytime/night time.

Figure 6 shows the diurnal cycle in the CO_2 forecast and observations at the ICOS (Integrated Carbon Observation System) tower at Cabauw in The Netherlands in June 2012. In the forecast, the day-time low-CO_2 values are consistently underestimated at all sampling levels;

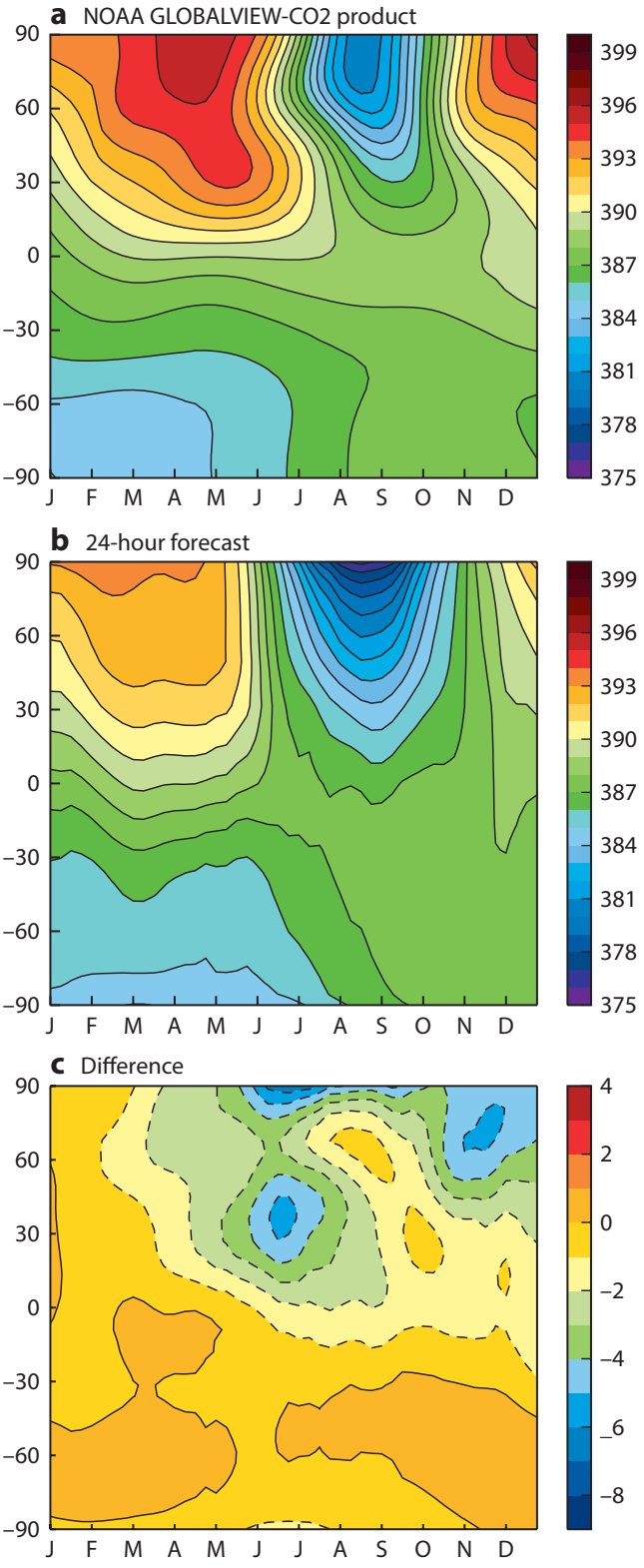

Figure 2 (a) NOAA GLOBALVIEW-CO2 product for 2010 based on observations, (b) the equivalent product based on the 24-hour forecast of CO_2, and (c) the difference between the GLOBALVIEW product and the forecast. The CO_2 forecast has been sampled at the same locations as the GLOBALVIEW observations and the same data processing described in *Masarie & Tans* (1995, *J. Geophys. Res.*, **100**, No. D6, 11593–11610) has been applied. Thanks to NOAA/ESRL for providing the GLOBALVIEW-CO2 product.

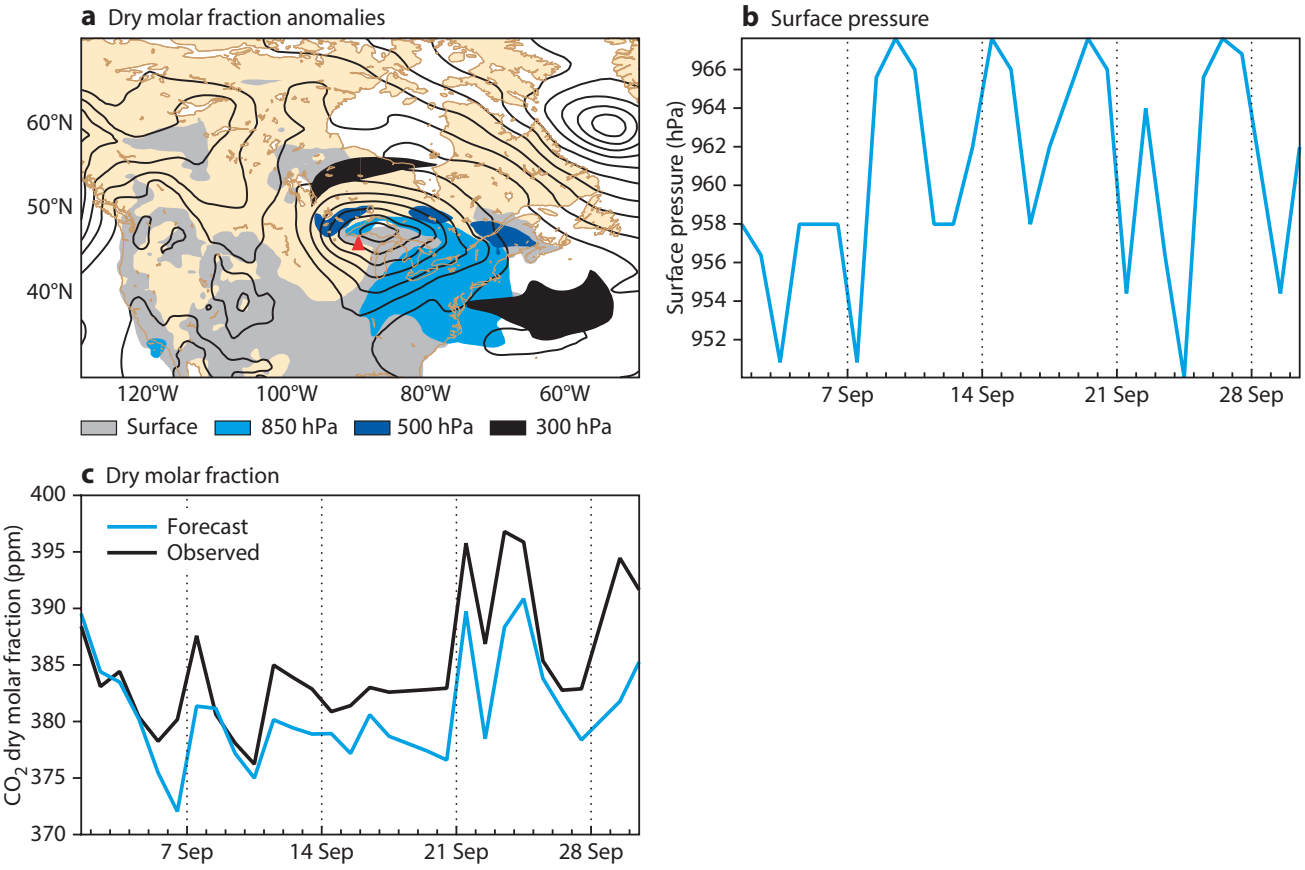

Figure 3 (a) CO_2 dry molar fraction anomalies [ppm]. Areas above above a threshold of 392 ppm at the 10-metre level are shaded in grey, areas above 392 ppm at the 850 hPa level are shaded in cyan, areas above 388 ppm at the 500 hPa level are shaded in blue and areas above 388 ppm at the 300 hPa level are shaded in black. Contours depict mean sea level pressure. The location of Park Falls is depicted by a red triangle. (b) ECMWF surface pressure forecast [hPa] and (c) daily mean CO_2 dry molar fraction [ppm] from the 24-hour forecasts in cyan and observed CO_2 in black at Park Falls in September 2010. Thanks to Arlene Andrews (NOAA/ESRL) for providing the CO_2 observations from the top level (396 m) of the ESRL/NOAA tall tower (*Andrews et al.*, 2013, *Atmos. Meas. Tech. Discuss.*, **6**, 1461–1553) at Park Falls (45.95°N, 90.27°W, 472 m a.s.l, Winsconsin, USA).

whereas at night-time, the forecast errors are not consistent at all sampling heights. This can be explained by the decoupling between lower and upper sampling heights during night-time stable conditions when the boundary layer collapses. Close to the surface, the night-time atmospheric CO_2 peak is also much more variable than the day-time CO_2. This large atmospheric CO_2 variability at night-time is associated with a strong coupling between the night-time CO_2 emissions and the decrease in the boundary layer height. Therefore, the CO_2 forecast can also be useful as an extra diagnostic in assessing the boundary layer turbulent mixing in the IFS, particularly in stable night-time conditions.

Uncertainties and future developments

As the CO_2 forecast is not constrained by CO_2 observations, it is globally biased. The offset is largest in the northern hemisphere and is associated predominantly with errors in the land vegetation fluxes in northern hemisphere mid-latitudes, particularly during the growing season. Despite the biases, overall the forecast simulates well the CO_2 synoptic variability modulated by the coupling between meteorological forcing of the fluxes and transport. Even during the spring months, when the synoptic variability in the model does not correlate well with the observed variability, there are significant correlations between meteorological parameters and observed CO_2. This implies that there is scope to improve the model. These model uncertainties will be addressed in the near future as part of the ongoing efforts to upgrade the real-time CO_2 forecasting system of the future Copernicus atmospheric service.

Data access and near-real-time monitoring

The CO_2 observations provided in near real time by the operational ICOS network are invaluable for the monitoring of the CO2 forecast. Continuous near-real-time monitoring of the MACC-II CO_2 forecast based on the pre-operational ICOS network is available online.

- http://www.gmes-atmosphere.eu/d/services/gac/verif/ghg/icos/

This evaluation supports the ongoing assessment of the model errors. It is also the first step towards assimilating in situ CO_2 observations into the forecasting system. In

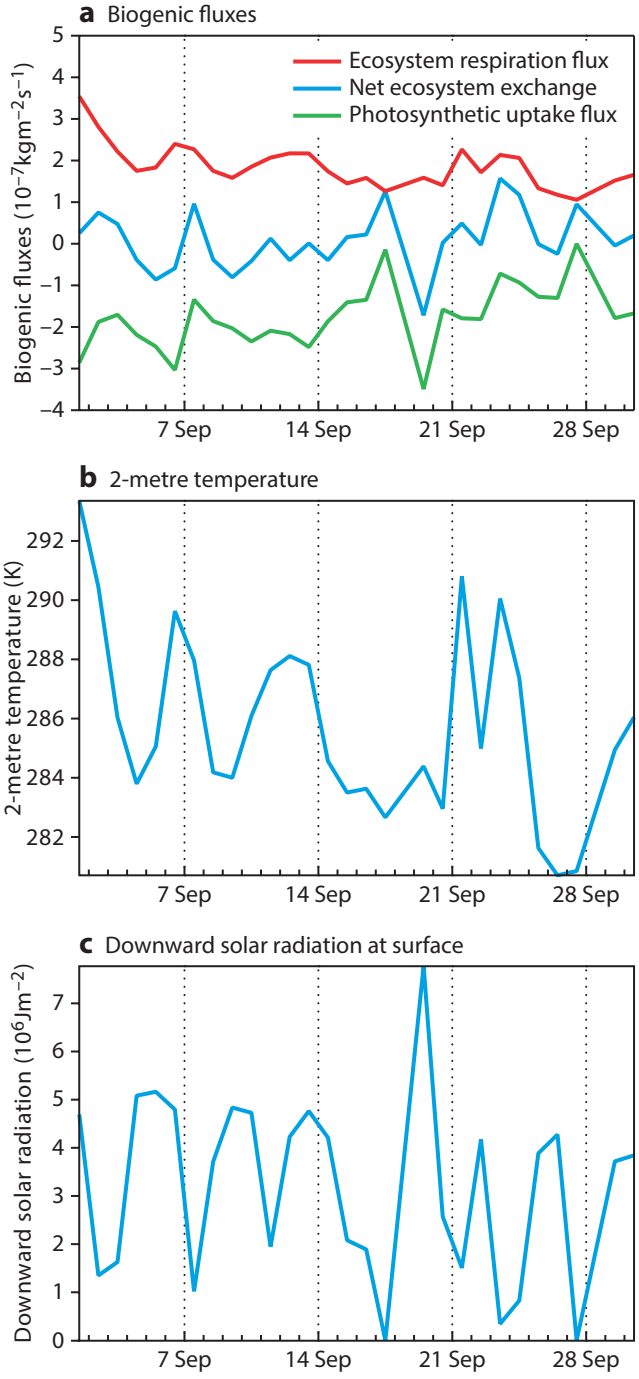

Figure 4 (a) Daily mean biogenic fluxes: net ecosystem exchange in cyan, photosynthetic uptake fluxes in green and ecosystem respiration fluxes in red [kg m^{-2} s^{-1}], (b) daily mean 2-metre temperature [K] and (c) daily mean downward solar radiation at the surface [J m^{-2}] from the 24-hour forecast at Park Falls in September 2010.

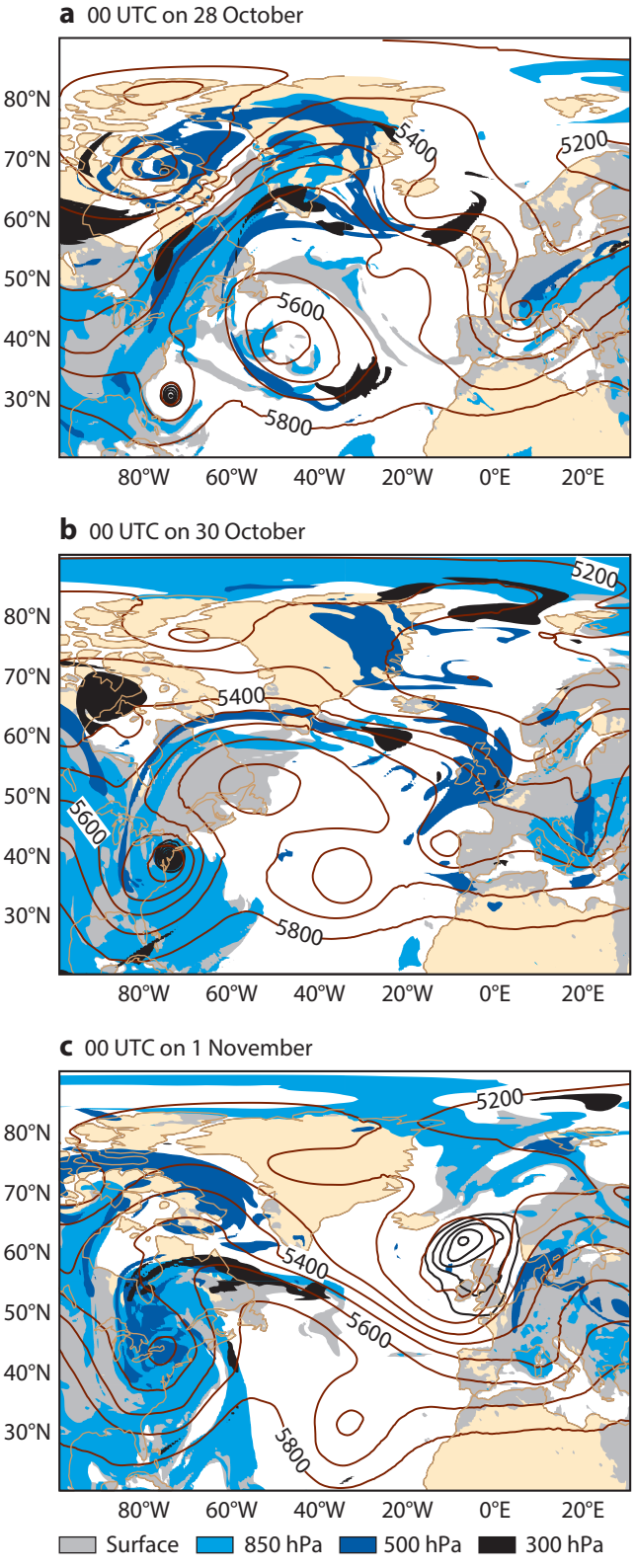

Figure 5 CO_2 dry molar fraction anomalies [ppm] depicting the landfall of Hurricane Sandy on (a) 28 October, (b) 30 October and (c) 1 November 2012. Areas above a threshold of 392 ppm are shaded in grey for the 10-metre level, in cyan for the 850 hPa level, in blue for the 500 hPa level and in black for the 300 hPa level. Brown and black contours depict geopotential height at 500 hPa and mean sea level pressure below 980 hPa respectively.

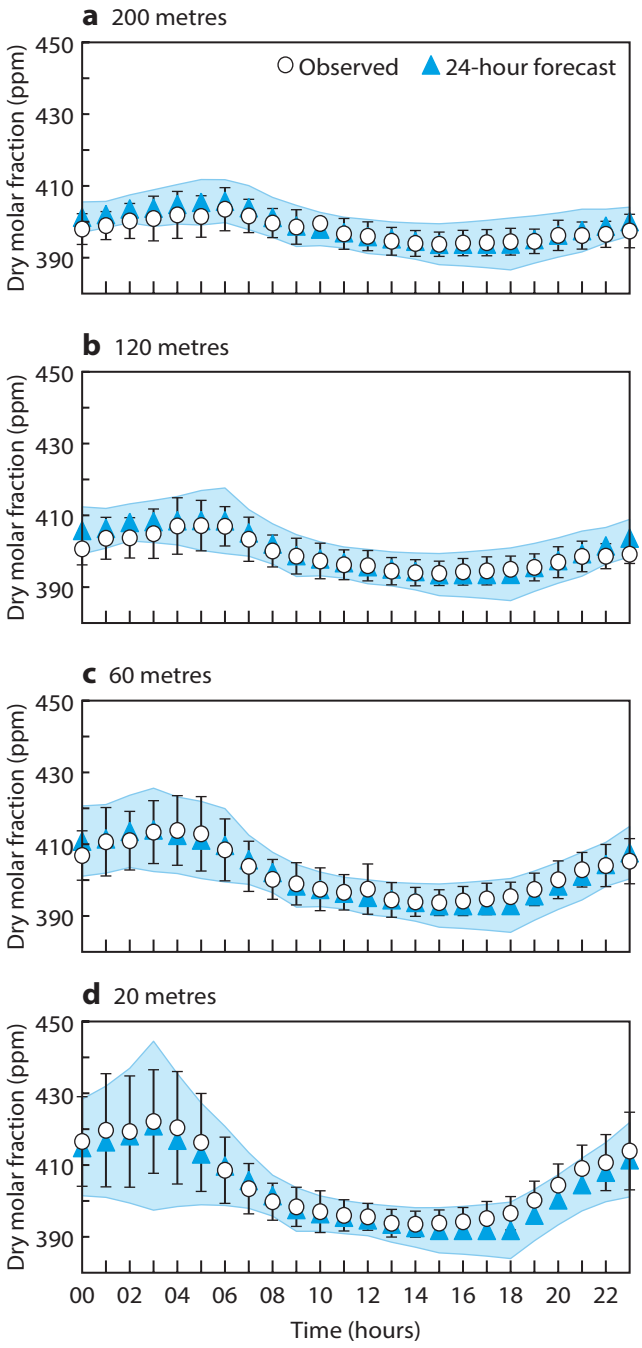

Figure 6 Mean diurnal cycle of CO_2 dry molar fraction [ppm] at four levels at the ICOS tall tower at Cabauw (51.97°N, 4.93°E, Netherlands) from measurements (circles) and 24-hour forecast (blue triangles) in June 2012. The standard deviations of observation and forecast day-to-day variability are shown as black bars and blue shading respectively. Thanks to Jérôme Tarniewicz (ICOS Atmospheric Thematic Center), and Philippe Ciais and Michel Ramonet (Laboratoire des Sciences du Climat et l'Environnement) for providing the data for MACC-II from the website at https://icos-atc-demo.lsce.ipsl.fr, as well as Alex Vermeulen (Energy research Centre of the Netherlands, ECN), the Principal Investigator from Cabauw station. The authors acknowledge the European Commission for the support of the preparatory phase of ICOS (2008–2013) and the Netherlands Ministry of Infrastructure and the Environment and ECN for the support of the observations at Cabauw.

return, the daily CO_2 forecasts prove very valuable for the ICOS data providers by allowing a better large-scale interpretation of the time series at the various observation locations.

Global maps of the 5-day forecast, run every day from 00 UTC, can be accessed online

- http://www.gmes-atmosphere.eu/d/services/gac/nrt/nrt_fields_co2/

The real-time global CO_2 forecast data is also available in the MACC-II data catalogue

- http://www.gmes-atmosphere.eu/catalogue/

We have seen that despite the biases associated mainly with the biogenic flux errors, the CO_2 forecast has skill in representing variability at synoptic scales. We are currently exploring the assimilation of CO_2 in situ and satellite retrievals in the IFS. However, in order to deliver a CO_2 analysis product in near real time, it is crucial that as many CO_2 observations and retrievals as possible are provided in near real time.

As well as the forecast of CO_2 supporting a variety of applications, we hope it will also be useful for regional modelling of CO_2 and future NWP developments. These include the evaluation of boundary layer mixing, the coupling of CO_2 with radiation in the NWP forecast and analysis, and the modelling of evapotranspiration.

FURTHER READING

Boussetta, S., G. Balsamo, A. Beljaars, A. Agustí-Panareda, J.-C. Calvet, C. Jacobs, B. van den Hurk, P. Viterbo, S. Lafont, E. Dutra, L. Jarlan, M. Balzarolo, D. Papale & **G. van der Werf**, 2013: Natural carbon dioxide exchanges in the ECMWF Integrated Forecasting System: Implementation and offline validation. *ECMWF Tech. Memo. No. 675*.

Chevallier, F., P. Ciais, T.J. Conway, T. Aalto, B.E. Anderson, P. Bousquet, E.G . Brunke, L. Ciattaglia, Y. Esaki, M. Fröhlich, A. Gomez, A.J. Gomez-Pelaez, L. Haszpra, P.B. Krummel, R.L. Langenfelds, M. Leuenberger, T. Machida, F. Maignan, H. Matsueda, J.A. Morguí, H. Mukai, T. Nakazawa, P. Peylin, M. Ramonet, L. Rivier, Y. Sawa, M. Schmidt, L.P. Steele, S.A. Vay, A.T. Vermeulen, S. Wofsy & **D. Worthy**, 2011: CO_2 surface fluxes at grid point scale estimated from a global 21-year reanalysis of atmospheric measurements, 2010: *J. Geophys. Res.*,**115**, D21307, doi:10.1029/2010JD013887.

Denning, A.S., T. Takahashi & **P. Friedlingstein**, 1999: Can a strong atmospheric CO_2 rectifier effect be reconciled with a "reasonable" carbon budget?, *Tellus*, **51B**, 249–253.

GLOBALVIEW-CO2, 2011: Cooperative Atmospheric Data Integration Project – Carbon Dioxide. NOAA ESRL, Boulder, Colorado (Available at http://www.esrl.noaa.gov/gmd/ccgg/globalview/).

Parazoo, N.C., A.S. Denning, J.A. Berry, A. Wolf, A.D. Randall, S.R. Kawa, O. Pauluis & **S.C. Doney**, 2011:

Convection and waves on small planets and the real Earth

PETER BECHTOLD, NOUREDDINE SEMANE, SYLVIE MALARDEL

The ECMWF plans foresee a horizontal resolution upgrade to T2047 (10 km) in 2015, and moving toward T3999 (5 km) around 2020. Exploratory forecasts at T7999 resolution (equivalent to about 2.5 km horizontal gridlength) have recently been presented by *Wedi et al*. (2012). The particular challenge at such high resolutions is that deep convective motions become gradually more resolved. Consequently the optimal partitioning in the model between resolved and sub-grid vertical motions and condensation processes has to be reconsidered. Also one wants to estimate the horizontal resolution beyond which the global forecasting system could eventually be run without a deep convection parametrization whilst improving the forecast skill on the medium to monthly time scales for both middle-latitude and tropical regions.

At the high resolutions being envisaged, not only the simulations but also the data storage and processing are extremely costly, rendering extensive experimentation and developments impractical on current computer systems. In order to overcome these limitations, *Wedi & Smolarkiewicz* (2009) set up a prototype reduced planet version of the atmospheric model used in the Integrated Forecasting System (IFS) without model physics. This enabled the development and efficient evaluation of the non-hydrostatic dynamical core of the model. The small-scale prototype approach is extensively used in the engineering community where, for example, the aerodynamic properties of a small-scale object are experimentally determined in a wind tunnel, and the performance data can then be up-scaled to the true sized object via a numerical model that is written in non-dimensional form.

Our goal is to develop a scaled version of the IFS with full physics that not only allows the model to be applied to planets of different size and gravity, but also faithfully reproduces the general circulation of the Earth. The final goal will be to have a system that permits deep convective motions while maintaining a realistic large-scale circulation. Such a system, which necessarily involves some approximations, has been pioneered by *Kuang et al*. (2005), *Pauluis et al*. (2006) and *Garner et al*. (2007), but has never been developed for a complex numerical weather prediction system.

In the following we present step by step, with increasing complexity, the various reduced planet configurations that have been used, and illustrate what each configuration can and cannot do.

Aqua planet and scaling laws

An ideal prototype is the Aqua planet. In this configuration, as proposed by *Hoskins & Neale* (2000), the whole planet is covered by water and the sea surface temperatures (SSTs) are specified. For an Earth-like simulation, typically a zonally symmetric SST distribution is chosen peaking at 27°C at the equator and decreasing to 0°C beyond 60° latitude. Furthermore, the Sun is fixed over the equator, thus there is no seasonal cycle. The advantage of the Aqua planet is that it removes complications due to land-surface/atmosphere interactions such as orographic drag, soil hydrology and the diurnal cycle over land. Also it avoids the complications of scaling the orography and height of the vegetation for planets of different size.

The reduced planet system has the following scalings.

- Horizontal length scale. The Earth's radius R_a is divided by a factor γ_R, and consequently the horizontal length scale L is also reduced by the same factor.
- Vertical length scale. The vertical length scale Z is conveniently reduced by a factor γ_g by increasing the gravity by the same factor, recognizing that the scale height H of the atmosphere is given by the ratio of a mean temperature T times the gas constant R and the gravity g.
- Time scale. The time scale t is reduced by a factor γ_Ω by increasing the rotation rate Ω of the planet by a factor γ_Ω which is equivalent to reducing the length of the day.

Consequently, choosing various values for the factors γ_R, γ_g and γ_Ω allows a choice of configurations. For example, the full Aqua planet has $\gamma_R = \gamma_\Omega = \gamma_g = 1$. More detailed information about the scaling is given in the Appendix.

While applying these scalings, the atmospheric motions on the reduced planet can be faithfully reproduced with respect to the full planet only if the two non-dimensional numbers, namely the Rossby and Richardson numbers, are kept constant. The Rossby number measures the ratio between the acceleration and the Coriolis force or rotational acceleration, while the Richardson number measures the relative importance of the buoyancy acceleration to the acceleration due to vertical advection (i.e. the importance of convection through the Brunt Väisälä frequency). Finally the Rossby and Richardson numbers can be cast into one single parameter, the Lamb parameter, which can be interpreted as the ratio between the planet rotational speed and the internal gravity wave phase speed. Interestingly, the Lamb parameter does not involve the horizontal wind speed which is an internal parameter. This means that when conserving the Lamb parameter, the wind field on the reduced planet is the same as on the full planet.

Isolated thunderstorm on a reduced planet

The first example is the simulation of an isolated split thunderstorm that evolves into a supercell thunderstorm. This is achieved by initialising the model with a convectively unstable sounding with rotational wind shear that is the same everywhere.

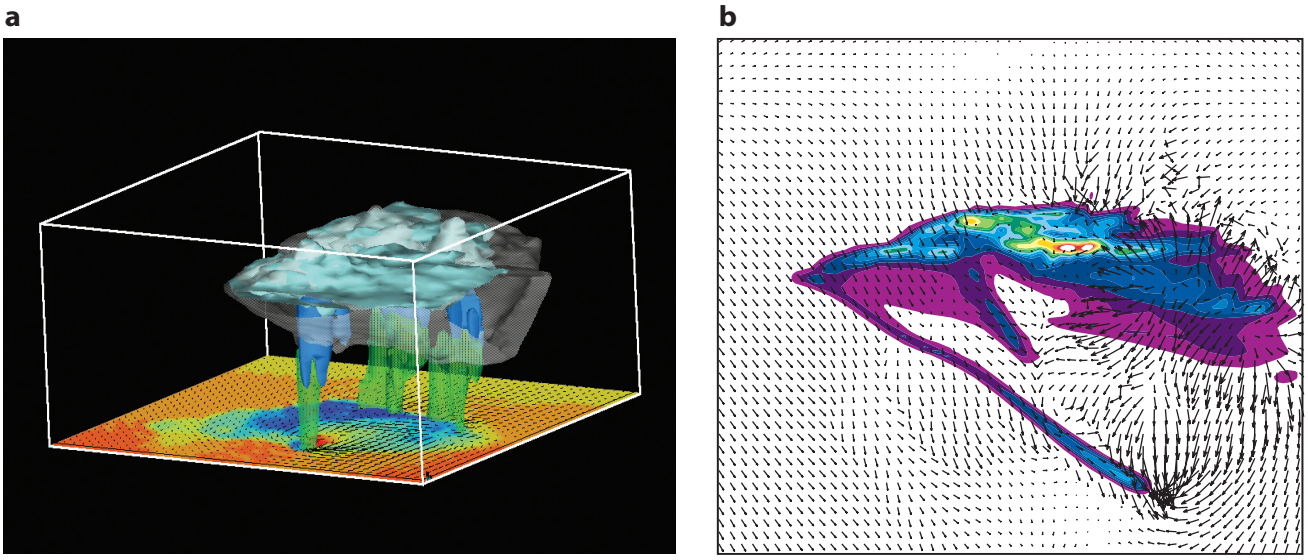

Figure 1 Non-hydrostatic simulation after 2 hours at resolution T511 with $\gamma_R = 12.5$ (3 km resolution) and $\gamma_g = \gamma_\Omega = 1$ in an environment with rotational wind shear. (a) Temperature (colour shading) and wind at the first model level, as well as the 0.5 g kg^{-1} iso-surfaces of cloud droplets (blue), cloud ice (cyan), rain (green) and snow (white). (b) Accumulated surface precipitation and low-level winds; the contour interval is 0.5 mm. The vortex to the right (right mover) is characteristic of vortices that in nature favour the formation of tornadoes.

The non-hydrostatic version of the IFS is run for two hours with full physics, but without deep convection parametrization at truncation T511. For this experiment, the Earth's radius is scaled by a factor $\gamma_R = 12.5$, giving an effective horizontal resolution of about 3 km, but the vertical length and time scales are not changed (i.e. $\gamma_g = \gamma_\Omega = 1$). This means that convective systems have the same size as on the real planet, while occupying a larger portion of the reduced planet.

Figure 1a shows the temperature and wind at the first model level along with the three-dimensional distribution of hydrometeors (i.e. cloud droplets, cloud ice, rain and snow). Also the accumulated surface precipitation and low-level wind is shown in Figure 1b. The results can be directly compared to corresponding simulations with limited area models because, given the small size of convective systems, the Coriolis effects due to the planet's rotation can be neglected. From these results it can be concluded that the reduced planet version of the IFS can be used to simulate intense isolated thunderstorms.

In this somewhat academic study we have indeed saved roughly a factor γ_R^2 (about 156) in computer time and data storage with respect to the actual 3 km full planet version of the model. However, by only scaling the planet radius, it is not possible to realistically represent the large-scale circulation or the interaction between the convective and synoptic-scale motion systems.

Dry baroclinic waves on the super-rotating planet

The synoptic scales on the reduced planet can only be faithfully reproduced with respect to the full planet if the Lamb parameter is conserved. This means that the rotation rate of the reduced planet has to be increased accordingly, so that both the characteristic wavenumber and frequency of the planetary Rossby waves remain unchanged.

To illustrate the scaling of dry synoptic waves, we employ a dry baroclinic test case following *Jablonowski & Williamson* (2006), where the model is initialised with a meridional temperature gradient and a geostrophically-balanced wind field with a strong zonal upper-level jet. The hydrostatic dynamical core of the model is then run without moist physics for ten planetary rotations at truncation T159, with the vertical length scale unchanged ($\gamma_g = 1$) and the other scaling factors as follows.

- $\gamma_R = \gamma_\Omega = 1$ which correspond to a 125 km horizontal resolution and rotation rate of 24 hours or 86,400 s (Figure 2a).
- $\gamma_R = \gamma_\Omega = 1{,}000$ which correspond to a 125 m horizontal resolution and rotation rate of 86.4 s (Figure 2b).

The results in Figure 2 show that the synoptic waves are quasi-identical in both simulations, indicating that the scaling is correct. However, nothing has been gained from the reduced planet simulations in terms of computer time and data storage; with respect to the full planet simulations the length of the integrations is still ten rotations, but the length of the day and the model time step have to be reduced accordingly. Furthermore, no model physics has been used in these planetary simulations. Had we done so, Figures 2a and 2b would no longer be identical. The reason being that, as the time scale of the synoptic forcing has been shortened, the physics also has to be accelerated. This is discussed next.

The global circulation and the shallow atmosphere

The most effective way to accelerate the physics consistently with the shortening of the synoptic flow time-scale is by scaling the gravity. This leads to a system where the horizontal length, vertical length and time scales are all reduced by the same factor (i.e. $\gamma_R = \gamma_\Omega = \gamma_g = \gamma$) – this is referred to as SASE (Shallow Atmosphere Small Earth).

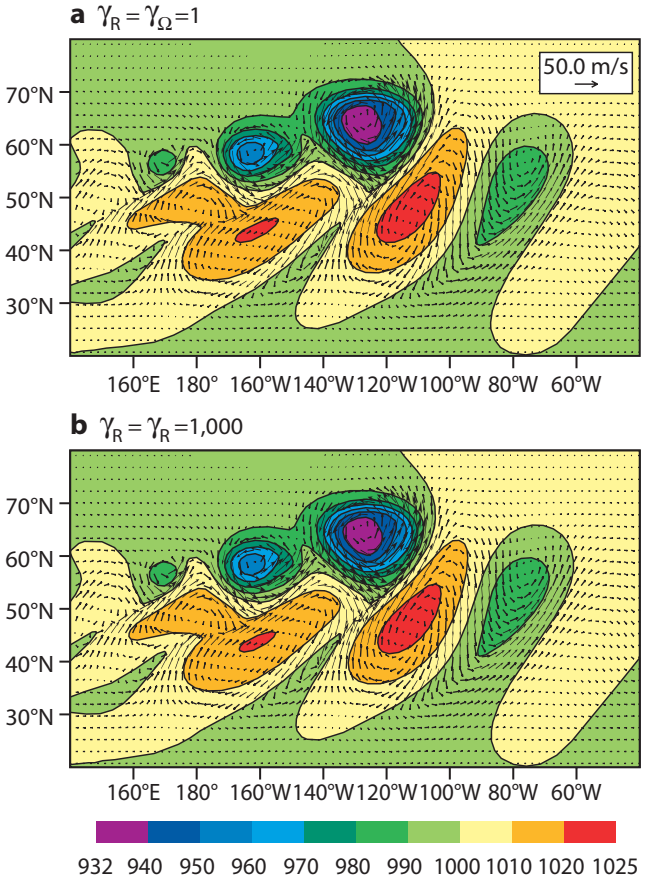

Figure 2 Baroclinic wave train with surface pressure contours (hPa) and wind field, in hydrostatic simulations at resolution T159 with $\gamma_g = 1$ and (a) $\gamma_R = \gamma_\Omega = 1$ (125 km resolution and 86,400 s rotation rate) and (b) $\gamma_R = \gamma_\Omega = 1{,}000$ (125 m resolution and 86.4 s rotation rate) after ten rotations of the planet. As the rotation rate of the planet has also been increased by a factor γ_Ω, (a) corresponds to a real time of 864,000 s and (b) to a real time of 864 s.

In this system with reduced scaled height, the diabatic forcing is naturally increased through radiative and surface heating as is the response through stratiform heating and convective heating and transport. Note that this system gives results that are identical to those in Figure 2 for the dry baroclinic wave case. However, a few precautions have to be taken in the physics concerning the internal constants that have been given absolute values instead of generally scaled values. In the model this affects the microphysical time-scales which have to be scaled by γ_Ω, as well as the turbulent length scale, and the entrainment and detrainment rates in the convection parametrization. The latter had to be rescaled by γ_g as the scale height of the atmosphere has been reduced.

The general circulation on the Aqua planet and its climate is simulated by starting from a balanced state, using a six-months spin-up forecast. A four-member ensemble is then generated by integrating the model for one year at spectral truncation T159. Figure 3a shows the annual mean precipitation (mm day^{-1}) on the real Earth as obtained from the GPCP2.2 dataset. The other panels in Figure 3 show the results for the full and reduced Aqua planet using the deep convection parametrization but different scalings.

- The full Aqua planet with $\gamma_R = \gamma_\Omega = \gamma_g = 1$ (Figure 3b) exhibits a distinctive tropical band with a precipitation rate of about 11 mm day^{-1}, and equatorially symmetric middle-latitude storm tracks. Its climate is in qualitative agreement with what is observed for the real Earth (Figure 3a).
- The reduced Aqua planet with $\gamma_R = \gamma_\Omega = 8$ and $\gamma_g = 1$ (Figure 3c), which has the same scaling as used for Figure

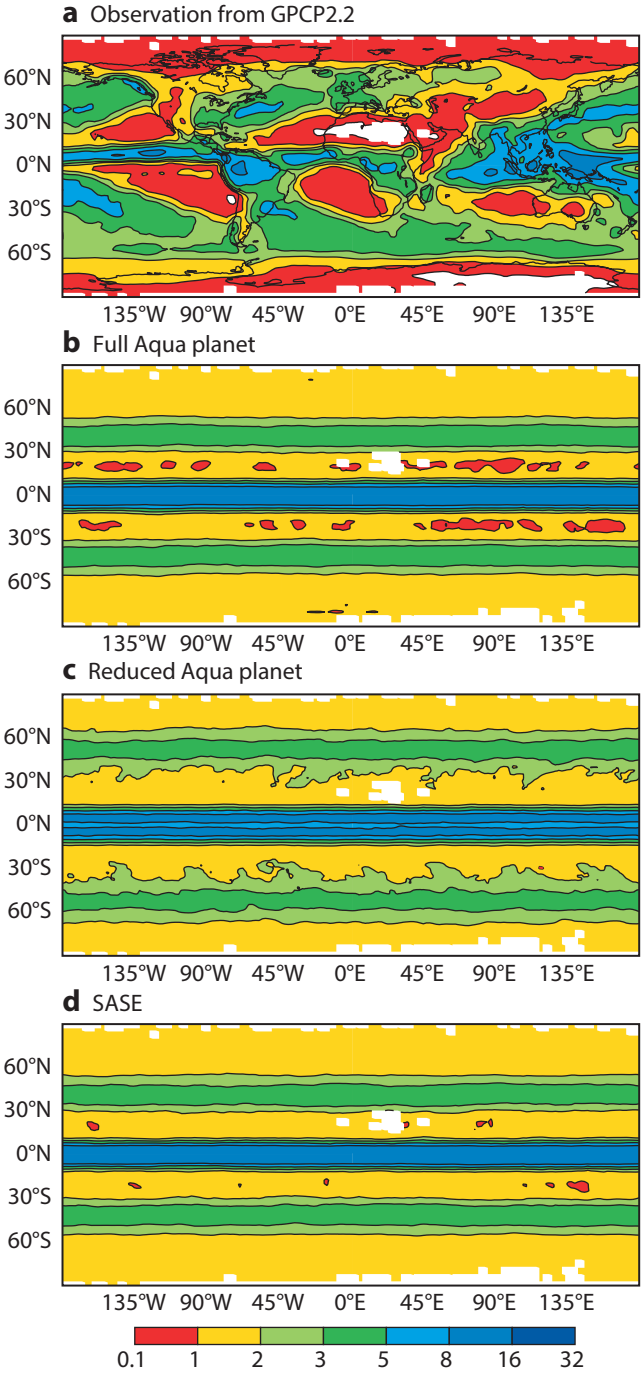

Figure 3 Annual mean daily global precipitation (mm). (a) Observations from the GPCP2.2 precipitation climatology dataset. Also shown are a one-year integration at T159 of a four-member ensemble with deep convection parametrization using (b) the full Aqua planet with $\gamma_R = \gamma_\Omega = \gamma_g = 1$, (c) the reduced Aqua planet with $\gamma_R = \gamma_\Omega = 8$ and $\gamma_g = 1$, and (d) the SASE system with $\gamma_R = \gamma_\Omega = \gamma_g = 8$.

2b, produces a split inter-tropical convergence zone and middle-latitude storm tracks that are shifted too far poleward. It is therefore not an accurate scaled version of the full Aqua planet.

- Using the SASE system with $\gamma_R = \gamma_\Omega = \gamma_g = 8$ (Figure 3d), an accurate small-scale version of the climate on the full planet is obtained.

The convectively-coupled waves in the tropical band are analysed in Figure 4 using wavenumber frequency diagrams of the outgoing longwave radiation. Satellite observations (Figure 4a) reveal the dominant tropical wave types which are the eastward propagating Kelvin waves and the westward propagating equatorial Rossby wave. The Madden-Julian oscillation is also apparent as a distinct mode. It can be seen that the dominant wave types are reasonably reproduced for the full Aqua planet simulations (Figure 4b), but the amplitudes are larger than those observed because these waves can freely circumnavigate the equator without being disturbed by land effects. However, the tropical wave spectra, and in particular the Kelvin waves, are heavily distorted for the reduced Aqua planet with $\gamma_R = \gamma_\Omega = 8$ and $\gamma_g = 1$ (Figure 4c), but faithfully reproduced with the SASE system using $\gamma_R = \gamma_\Omega = \gamma_g = 8$ (Figure 4d).

The SASE system is shown to provide the correct scaling of the full planet and therefore allows the model to be applied to planets of different size and gravity. Unfortunately, nothing has been gained in terms of computer time, and we have still not achieved our final goal of resolving deep convection. Indeed, in the SASE system the scale of the convection has also been reduced. This follows from observational evidence showing that the horizontal scale of convective clouds is related to the scale height. Also, from a scale analysis it follows that for SASE the time scale of convection has been reduced, but the vertical velocity is the same as for the full Aqua planet simulation.

Towards global resolved convection

Our final aim is to efficiently resolve deep convection on the reduced planet, while maintaining a realistic interaction between the convection and the large-scale circulation. The basic idea is to reduce the gap between the convective and large-scale motions. This can be achieved either by reducing the scale of the synoptic circulations, therefore bringing them closer to the convective scales, or by increasing the scale of the convective motions.

The former approach was proposed by *Kuang et al.* (2005) and called DARE (Diabatic Acceleration and Rescaling). In this system $\gamma_\Omega = \gamma_R = \gamma$ and $\gamma_g = 1$ with rescaling of the external forcings. In addition, we considered the alternative Deep Atmosphere Small Earth (DASE) approach, where DARE is combined with the scaling of the SASE system giving $\gamma_\Omega = \gamma_R = \gamma$ and $\gamma_g = \gamma^{-1}$. This means that the scale height of the atmosphere is increased with a consequent increase in the horizontal scale of convective motions – see Box A for more information.

Figure 5 displays the annual mean precipitation rate, similar to that shown in Figure 3, but for hydrostatic integrations without convection parametrization for:

- The full Aqua planet at truncation T159 and T1279 (Figures 5a and 5b).
- The reduced Aqua planet at T159 with γ=8 using the DARE and DASE configurations (Figures 5c and 5d).

The T159 integration without convection parametrization

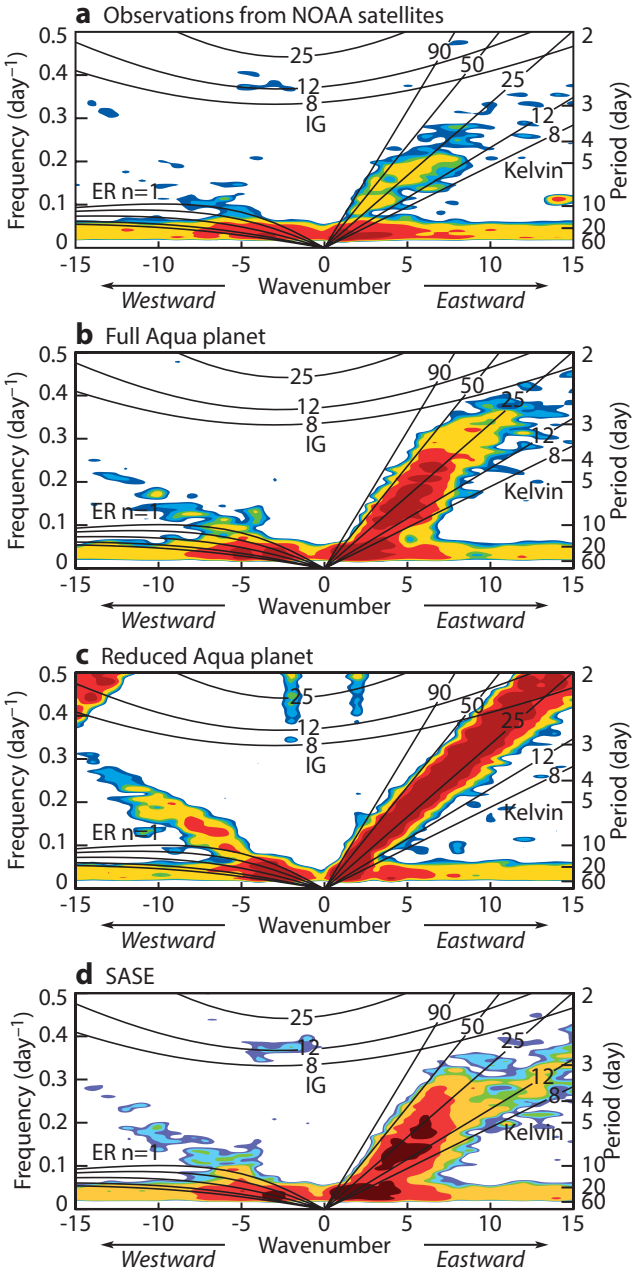

Figure 4 Same as Figure 3, but for the wavenumber frequency spectra of the outgoing longwave radiation with observations from the NOAA satellites. The data has been averaged between 10°S and 10°N, a background spectrum has been substracted, and only the symmetric part of the spectrum is displayed. Spectra include the theoretical dispersion relations with external gravity wave phase speed $c = (gH)^{1/2}$ as a function of equivalent depth H. The characteristic tropical wave types include the eastward propagating Kelvin waves, the westward propagating Equatorial Rossby (ER) waves, and the Inertia Gravity (IG) waves. Note that Kelvin waves behave like gravity waves, and that the Madden-Julian Oscillation corresponds to the spectral peak in the wavenumber 1–2 and period 20–60 days band.

(Figure 5a) greatly overestimates the equatorial precipitation compared to the control run with deep convection parametrization (Figure 3b). But, when increasing the resolution to T1279 (Figure 5b), the results without convection parametrization become comparable to the control.

If the DARE or DASE configurations at T159 (with γ=8 using the same time step as the T1279 integration) are able to reproduce the T1279 results, then we have indeed a system that allows a saving in computer time of order γ^3 (i.e. order 512). However, DARE (Figure 5c) essentially only reproduces the results of the T159 integration (Figure 5a). This was expected as we are not yet in the non-hydrostatic regime. In contrast, the results with DASE (Figure 5d) become comparable to the T1279 full planet integration and also to the T159 integration preformed with deep convection parametrization (Figures 3b and 3d).

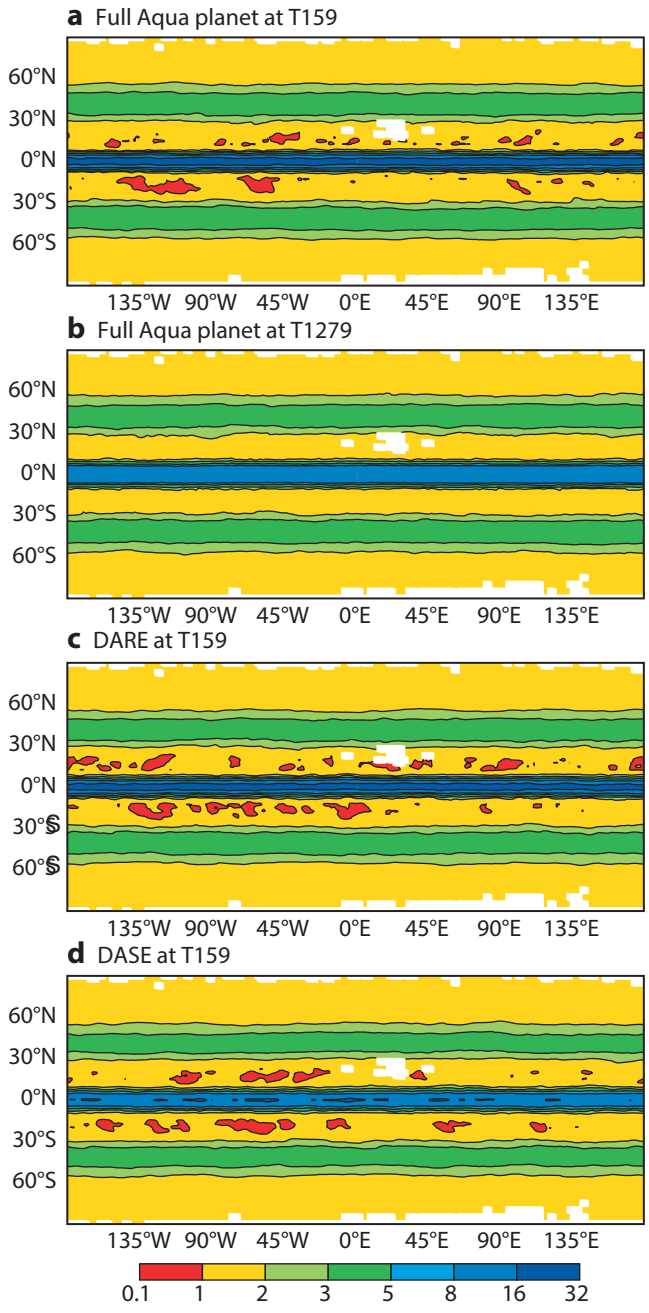

Figure 5 Annual mean daily global precipitation (mm) for hydrostatic integrations without deep convection parametrization for the full Aqua planet ($\gamma_R = \gamma_\Omega = \gamma_g = 1$) at (a) T159 and (b) T1279, and the reduced Aqua planet at T159 with (c) DARE ($\gamma_R = \gamma_\Omega = 8$ and $\gamma_g = 1$) and (d) DASE ($\gamma_R = \gamma_\Omega = 8$ and $\gamma_g = 1/8$).

As well as considering the distribution of precipitation, it is worthwhile examining whether DASE can produce realistic tropical wave spectra. Figure 6 displays the tropical wave spectra for the simulations illustrated in Figure 5. In the T159 integration without convection parametrization, as well as in DARE, the wave spectra are broad and noisy (Figures 6a and 6c). However, at T1279 (Figure 6b) the wave spectra become comparable to the integration with deep convection (Figure 3b).The dominant wave types are also reasonably reproduced with DASE (Figure 6d).

The results given in Figures 5 and 6 show that the new fully scaled system DASE is indeed a step forward in resolving convection as it is able to mimic both the mean climate and the wave motions of the T1279 full planet integrations.

DARE and DASE scaling

A

DARE (Diabatic Acceleration and Rescaling) uses $\gamma_\Omega = \gamma_R = \gamma$ and $\gamma_g = 1$, and requires the rescaling (acceleration) of the external forcing including radiation and surface fluxes in order to increase the forcing of convective-scale motions. A key aspect of DARE is that the vertical scale remains unchanged. Thus, even though the convection is driven more strongly by a factor γ_Ω, the natural horizontal scale of the convection is unchanged, and hence is a factor γ_Ω closer to the synoptic scale. Yet, DARE requires non-hydrostatic simulations to take advantage of the reduced synoptic/convective scale separation. In fact, the quasi-nonhydrostatic parameter, which scales as the square of the aspect ratio (i.e. H/L where H is the scale height and L is the horizontal length scale), is not large enough to allow a transition into the resolved range.

The Deep Atmosphere Small Earth (DASE) approach combines DARE with the scaling of the SASE system, but increases H by reducing gravity, and consequently increases the horizontal scale of convective motions. In DASE, we therefore have $\gamma_\Omega = \gamma_R = \gamma$ and $\gamma_g = \gamma^{-1}$.

While DASE increases the convective scales, and increases the aspect ratio and vertical motions by a factor γ_Ω^2, it also reduces the synoptic scales. The convective and synoptic motions are therefore closer in scales, and can be resolved simultaneously over a time-step equivalent to the one used in a simulation γ times wider in the horizontal direction, γ times narrower in the vertical direction and γ times longer in time. The quasi-non-hydrostatic condition becomes sufficiently large to allow a transition into the resolved range.

The DARE and DASE systems include the physics scaling with the radiative flux, surface heat and momentum fluxes, microphysical time scales, and fall velocity of precipitation.

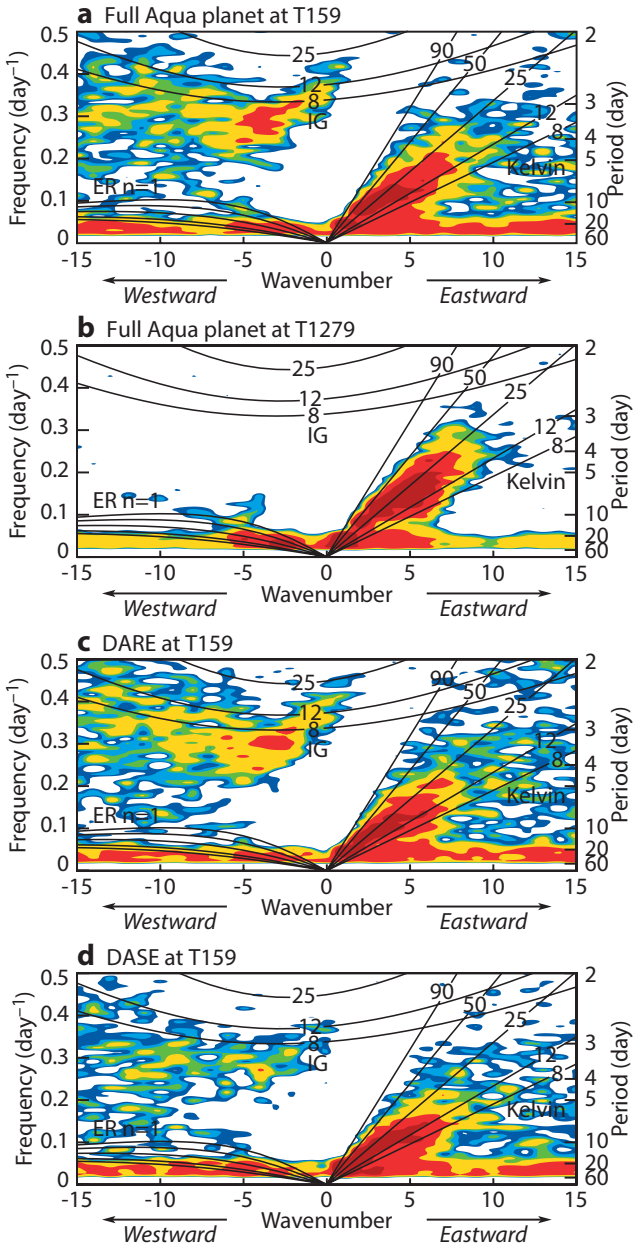

Figure 6 Same as Figure 4, but with wavenumber frequency spectra corresponding to the simulations in Figure 5.

Perspectives

A scaled version of the IFS has been developed; it can be applied to planets of different size and gravity. Also, a slightly different alternative system dubbed 'Deep Atmosphere Small Earth' opens the potential to efficiently mimic resolved deep convection. This constitutes ground-breaking research, and the prototype version will be available to users of OpenIFS from Cy39r1 onward. There are however evident limitations in the method in that it is not possible to rescale the micro-physical processes in a way that is consistent both with the small- and large-scale processes. We estimate that values of γ up to 10 might still provide sufficient physical realism, while providing efficient high-resolution experimentation. In particular, we intend to study the transition from parametrized to resolved convection in the 10 km to 1 km resolution range, and the effects of convectively generated gravity waves on the circulation in the stratosphere and mesosphere.

Appendix. Scaling parameters and non-dimensional numbers

External control: Scaling parameters

Scaling of the external planetary parameters, planetary radius R_a, gravity g, and rotation speed Ω by a factor γ leads to the scaling of horizontal length L, height scale Z and time scale t as follows.

$$R'_a = R_a / \gamma_R \quad \rightarrow \quad L' = L / \gamma_R$$

$$g' = g\gamma_g \quad \rightarrow \quad H' = \frac{RT}{\gamma_g g} \rightarrow H / \gamma_g \rightarrow Z' = Z / \gamma_g$$

$$\Omega' = \Omega\gamma_\Omega \quad \rightarrow \quad t' = t / \gamma_\Omega$$

Here T is the mean temperature and R the gas constant.

Non-dimensional characteristic numbers

Non-dimensional numbers can be derived that include the Rossby number, Ro, the Richardson number, Ri, and the Lamb parameter, La, involving also the Brunt Väisälä frequency N and the internal gravity wave phase speed c.

$$N^2 = \frac{g}{\theta}\frac{\Delta\theta}{H} \qquad c = NH$$

$$Ro = \frac{U}{2\Omega R_a} \qquad Ri = \frac{N^2H^2}{U^2} \rightarrow \quad La = Ro^{-2}Ri^{-1} = \frac{4\Omega^2R_a^2}{c^2}$$

FURTHER READING

Garner, S.T., **D.M.W. Frierson**, **I.M. Held**, **O. Pauluis** & **G.K. Vallis**, 2007: Resolving convection in a global hypohydrostatic model. *J. Atmos. Sci.*, **64**, 2061–2075.

Jablonowski, **C.** & **D.L. Williamson**, 2006: A Baroclinic Instability test case for atmospheric model dynamical cores. *Q. J. R. Meteorol. Soc.*, **132**, 2943–2975.

Kuang, Z., **P.N. Blossey** & **C.S. Bretherton**, 2005: A new approach for 3D cloud-resolving simulations of large-scale atmospheric circulation. *Geophys. Res. Letters*, **32**, L02809.

Neale, **R.B.** & **B.J. Hoskins**, 2000: A standard test for AGCMs including their physical parameterizations. I: The proposal. *Atmos. Sci. Let.*, **1**, 101–107, doi:10.1006/asle.2000.0022.

Pauluis, **O.**, **D.M.W. Frierson** & **S.T. Garner**, 2006: The hypohydrostatic rescaling and its impact on modeling of atmospheric convection. *Theor. Comput. Fluid Dyn.*, **20**, 485–499.

Wedi, **N.P.** & **P.K. Smolarkiewicz**, 2009: A framework for testing global non-hydrostatic models. *Q. J. R. Meteorol. Soc.*, **135**, 469–484.

Wedi, **N.P.**, **M. Hamrud**, **G. Mozdzynski**, **G. Austad**, **S. Ćurić** & **J. Bidlot**, 2012: Global, non-hydrostatic, convection-permitting, medium-range forecasts: progress and challenges. *ECMWF Newsletter No. 133*, 17–22.

Scaling of GNSS radio occultation impact with observation number using an ensemble of data assimilations

SEAN HEALY, FLORIAN HARNISCH,
PETER BAUER, STEVE ENGLISH

In *'The ECMWF Strategy 2011–2020'* one of the complementary goals is to contribute towards the optimisation of the Global Observing System (GOS) so that it meets the future needs of weather forecasting and climate monitoring. The evolution of the GOS should reflect updated user requirements, and the emergence of new – or recently demonstrated – technologies, which may complement the more established measurement techniques. The satellite component of the GOS is composed of a diverse set of complex observing systems, each with particular strengths, so optimising the future GOS requires finding a reasonable balance of these distinct measurement types.

Global Navigation Satellite System Radio Occultation (GNSS-RO) measurements complement the information provided by satellite radiances, and these measurements are of particular value in the upper troposphere and stratosphere because of their high vertical resolution. More information about the GNSS-RO measurement technique is given in Box A.

A question that has arisen in the context of designing the future GOS is how the impact of GNSS-RO measurements is likely to be enhanced if the number can be increased significantly above the 2,500 to 3,000 observations that are currently available. This is particularly relevant because new GNSS systems, such as Galileo, could increase the GNSS-RO observation number. ECMWF has recently completed a Galileo Science Study, funded by the European Space Agency (ESA), to address this question. This involved investigating the impact of up to 128,000 GNSS-RO observations per day (*Harnisch et al.*, 2013).

The Galileo Science Study supports the case for a considerable increase in the number of GNSS-RO measurements above the present day levels. More specifically, the results indicate that we should be aiming for at least 16,000 to 20,000 operational GNSS-RO measurements per day, in the coming years. These results have helped inform a recent revision of the WMO *'Vision for the Global Observing System in 2025'*.

Method

Estimating the impact of increasing the GNSS-RO observations requires the ability to simulate the measurements accurately, and then assess them within the context of a state-of-the-art numerical weather prediction (NWP) system. Their impact must be given relative to a reasonable GOS baseline, in order to obtain reliable and robust results that will remain relevant in the coming years.

The GNSS-RO measurement technique A

The figure shows the geometry of the GNSS-RO measurement technique. A radio signal is transmitted by a GNSS satellite, passes through the atmosphere and is measured with a receiver placed on a LEO satellite, such as the GRAS instrument on Metop-A. The path is bent as a result of gradients in the refractive index of the atmosphere, which in turn can be related to gradients in the temperature and humidity.

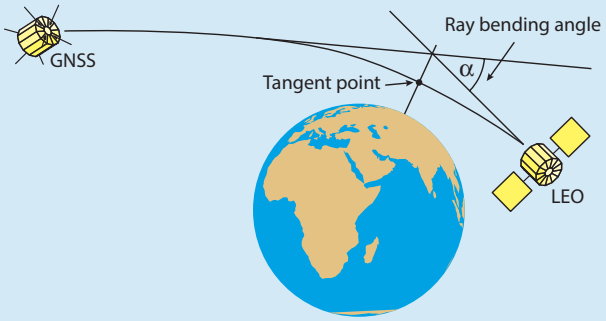

The geometry of a GNSS-RO measurement. A radio signal is emitted by the GNSS satellite and measured with a receiver placed on the low earth orbit (LEO). The path of the radio signal is bent as a result of refractive-index gradients in the atmosphere. The motion of the LEO satellite enables the variation of ray-bending with tangent height to be derived.

The ray bending angle, α, can be derived from the time required for the radio signal to propagate between the GNSS and LEO satellites, and the motion of the LEO satellite enables the variation of α as a function of tangent height to be determined. Temperature, humidity and surface pressure information can be retrieved directly from the bending angle profiles within the 4D-Var framework. The limb sounding geometry of the measurements means that they have good vertical resolution, focussed on a few hundred kilometres around the horizontal location of the tangent point.

The measurements provide particularly good temperature information in the vertical interval between ~200 hPa to ~5 hPa. They are less sensitive to biases than satellite radiance measurements, because they are derived from a precise measurement of a time delay with an atomic clock. Consequently, the GNSS-RO measurements are assimilated without bias correction, and so they can 'anchor' the bias correction of satellite radiances.

One well-established approach for investigating the impact of the simulated data is to perform Observing System Simulation Experiments (OSSEs) (*Andersson & Masutani,* 2010). However, OSSEs require the simulation of all the observation types that are assimilated, and they are extremely computationally expensive. In this study we have used an alternative approach based on an Ensemble of Data Assimilations (EDA).

An EDA can be used to derive flow-dependent theoretical analysis and short-range forecast error covariance information (See *Isaksen et al.*, 2010). An ensemble of ten 4D-Var assimilations is run in parallel, but with perturbed observations, model physics and sea surface temperatures. If the perturbations are consistent with the actual error statistics of these variables, then the EDA will provide an accurate estimate of the analysis and short-range forecast error statistics – or uncertainty – of the NWP system. The uncertainty is estimated from the 'spread' of the ensemble, which is the standard deviation of the ensemble members about the mean of the ensemble. It is sometimes stated that ensembles provide 'errors of the day', but this is shorthand terminology and it can be misleading. More precisely, the ensembles provide estimates of the 'error statistics of the day'.

An EDA has been operational at ECMWF since July 2010, and it has had a significant impact on forecast scores (*Bonavita et al.*, 2012). Furthermore, *Tan et al*. (2007) have shown that the EDA can be used to assess the impact of new measurements. They demonstrated that simulated wind profiles from ESA's Earth Explorer Atmospheric Dynamics Mission (ADM-Aeolus) can be assimilated alongside real data in an EDA, and that the EDA spread values can be used to estimate the impact of the simulated data. The central idea is that if the new observations are going to have a positive impact, the estimate of the uncertainty should be reduced and thus the EDA spread values should be reduced.

EDA experiments

The EDA experiments have been performed for a six week period from 1 July to 15 August 2008. This period was chosen because it enabled comparison with a detailed set of GNSS-RO observing system experiments (*Bauer et al.*, 2013). The EDA spread values have been used to estimate the impact of 2,000, 4,000, 8,000, 16,000, 32,000, 64,000 and 128,000 simulated GNSS-RO observations, relative to a baseline observing system that assimilates all the non GNSS-RO observations that were used operationally during the period of the experiment. It is worth noting that although 128,000 observations per day is considered a very dense network of GNSS-RO measurements, the mean spacing between observations in an hour is still about 300 km.

Two additional EDA experiments have also been performed for comparison purposes: one assimilating real GNSS-RO measurements, and the other assimilating neither simulated nor real GNSS-RO measurements.

The simulated GNSS-RO observations are generated using ECMWF operational analyses (see Box B). They are assumed to be randomly distributed in both space and time. This simplification means that we do not perform any satellite orbit modelling in order to calculate the observation locations. Random noise is added to the simulated data to simulate observation error.

The simulated GNSS-RO measurements are subsequently assimilated in the EDA experiments assuming the same observation error statistics that are used operationally at ECMWF. The EDA spread values depend on the assumed observation error statistics used in the EDA system, rather than the actual observation error statistics. This may seem a rather subtle point, but it has been key to understanding

Some remarks, technical aspects and interpretation B

The technical details of the EDA experimentation are described in *Harnisch et al*. (2013). The simulated observations are produced with a two-dimensional (2D) observation operator, which accounts for the real limb geometry of the measurement by using the NWP information in a plane to compute the bending angles. The simulated GNSS-RO measurements are subsequently assimilated in the EDA experiments assuming the same observation error statistics that are used operationally at ECMWF, and using a one-dimensional (1D) operator which uses only the NWP profile information at the location of the observation.

The obvious inconsistency of simulating the observations with a 2D operator, but assimilating with a 1D operator was deliberate. Firstly, it reflects how the GNSS-RO measurements are currently used at most NWP centres. Furthermore, it was originally expected that this inconsistency would introduce correlated forward model errors, which would influence the spread values. However, this is not correct because the spread values are determined by the observation error statistics assumed in the EDA system that are used to generate the perturbations, rather than the actual errors on the simulated measurements. This fact can be related to well-known theory. For example, the theoretical error statistics provided by a linear Kalman filter depend only on the assumed observation and model error covariance matrices.

In general, we note that there are some clear similarities between this type of EDA calculation and the one-dimensional information content studies routinely used satellite meteorology. One-dimensional variational (1D-Var) retrievals usually provide a solution error covariance matrix. For example, these are often used in radiance channel selection studies. In the 1D-Var case, the covariance matrices can be computed explicitly, because they have relatively small dimensions, of order 100. In the 4D-Var case, the covariance matrices are much larger, because they relate to a full three-dimensional atmospheric state estimate, so they have to be approximated using the ensemble methods. We interpret the EDA spread results as a 4D-Var information content study.

many aspects of the study. For example, it explains why – unlike OSSEs – it is possible to use a mix of real and simulated data in the EDA approach, and also why the ECMWF analyses can be used for simulating the measurements.

The EDA provides a theoretical estimate of the analysis and short-range forecast error statistics, which are valid for the assumed observation error statistics. Clearly, the hope must be that the assumed and actual errors statistics are reasonably close for real measurements, and the fact that the real data is assimilated successfully would support this assumption. However, the error statistics used in the EDA for the simulated GNSS-RO measurements represent the characteristics we hope to obtain when the corresponding real data becomes available, rather than the actual, complex error statistics of the simulated data that is assimilated.

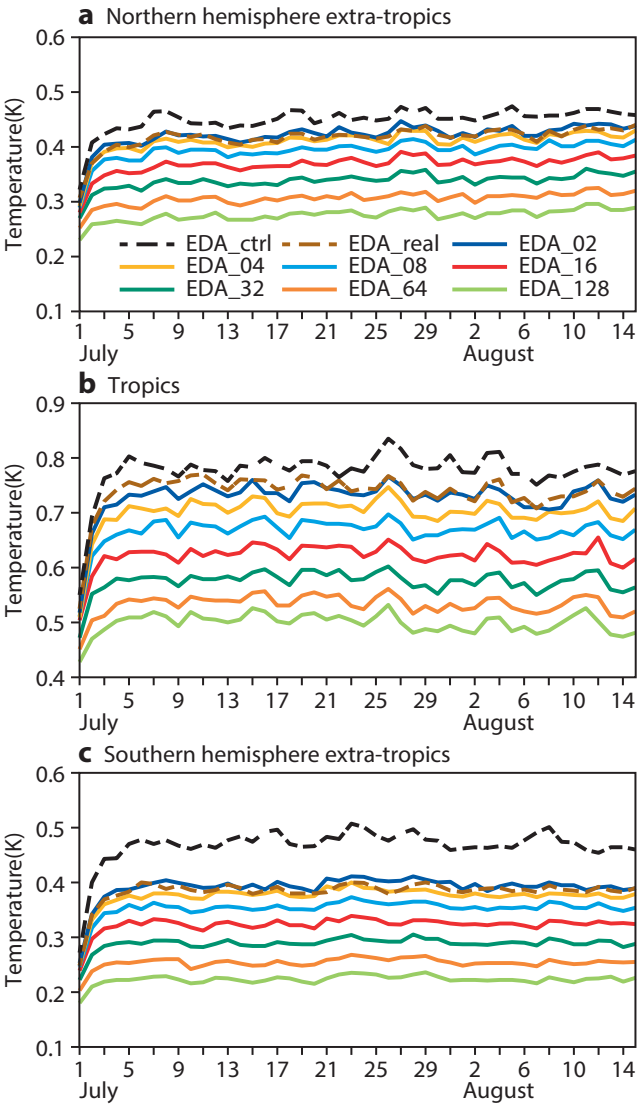

Figure 1 Time series for July to August 2008 of daily 12-hour forecast EDA spread values for temperature (K) at 100 hPa for (a) northen hemisphere extra-tropics, (b) tropics and (c) southern hemisphere extra-tropics. 'EDA_n', refers to the EDA experiment with 'n' thousand simulated GNSS-RO observations. EDA_ctl is the control experiment with no GNSS-RO measurements assimilated and EDA_real is with the real GNSS-RO data.

Main results with simulated GNSS-RO data

Figure 1 shows the time series for the EDA spread values for 12-hour temperature forecasts at 100 hPa, averaged over the (a) northern hemisphere extra-tropics, (b) tropics and (c) southern hemisphere extra-tropics. This is a fairly typical EDA time series, irrespective of the chosen variable or level. There is generally a spin-up period of roughly one week before the spread values reach a reasonably stable state, which is then maintained for the remainder of the experiment. The increase in the EDA spread during the early stages is because the EDA members are 'cold started' from the same initial forecast state. The subsequent stability of the EDA spread values is because they approximate the forecast error statistics, rather than the forecast errors themselves. This stability of the EDA spread values has important practical implications, suggesting that it is not necessary to run extremely long experiments to test new measurements with this approach.

The vertical profiles of the EDA spread values of the temperature analyses are shown in Figure 2. These are averaged for the period 8 July to 15 August 2008 to remove the spin-up period. The inclusion of the either real or simulated measurements reduces the spread values compared to a control experiment, where GNSS-RO measurements are not assimilated. In general, there is good agreement between the EDA spreads produced by the ~2,500 real GNSS-RO observations (EDA_real) and 2,000 simulated measurements (EDA_02). The small differences in these spread values can be attributed to the random spatial sampling assumed when generating the simulated data, which produces a slightly different latitudinal distribution for real and simulated data, as shown in Figure 3. The largest reductions in the spread values are in the upper-troposphere and lower/middle-stratosphere, where the GNSS-RO information content is known to be greatest. The spread values continue to reduce as more GNSS-RO measurements are added, even for observation numbers greater than 32,000 per day (EDA_32).

We have been able to compare the EDA results with a comprehensive set of GNSS-RO observing system experiments (OSEs) conducted over the same period. These OSEs were designed to investigate whether there is any indication of saturation of forecast impact with the currently available GNSS-RO observation numbers, and they looked at the impact of assimilating 0, 5, 33, 66 and 100% of the available observations. The 100% coverage in the OSEs represents an average of 2,450 real observations per day. Figure 4 shows a comparison of the OSE results with the EDA spread values for the 24-hour temperature error at 100 hPa. In both cases the results are 'normalized' with their result when the GNSS-RO measurements are not assimilated. There is reasonably good agreement between the two approaches for low observation numbers and this result provides us with additional confidence in the EDA results.

Figure 5 shows the normalized EDA spread as a function of GNSS-RO observation number for temperature, geopotential height and relative humidity on various fixed pressure levels. Again, the normalization is performed by dividing

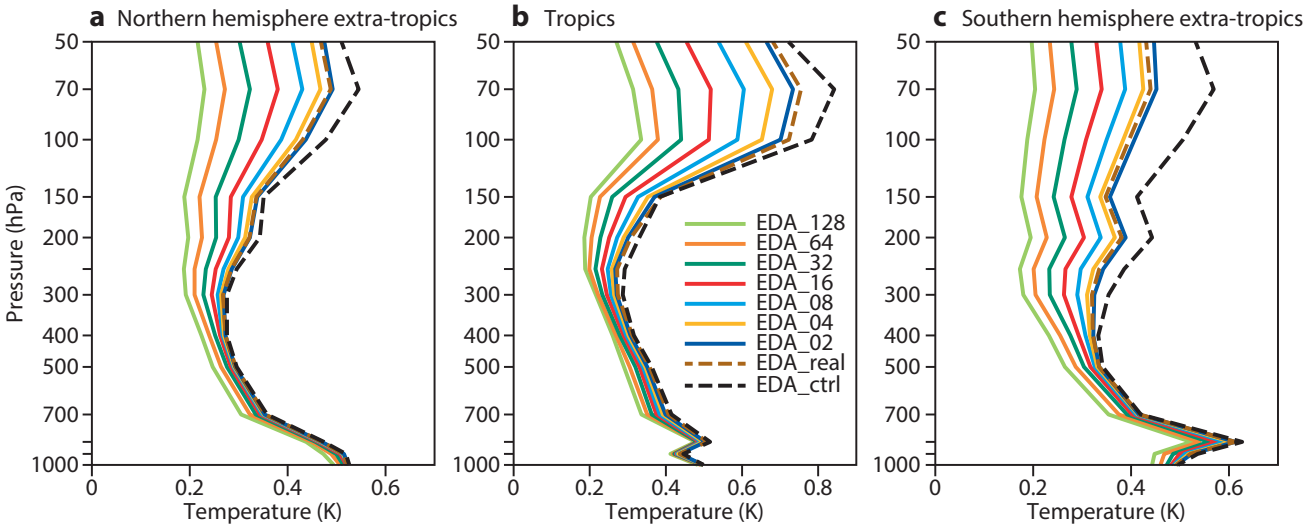

Figure 2 EDA spread for temperature (K) at analysis time averaged over (a) northern hemisphere, (b) tropics and (c) southern hemisphere. Results are for the period 8 July 2008 to 15 August 2008. As with Figure 1, 'EDA_n', refers to the EDA experiment with 'n' thousand simulated GNSS-RO observations, EDA_ctl is the control and EDA_real is with the real GNSS-RO data.

each spread value by the no GNSS-RO result. The continued reduction in the spread values is clear when the results are plotted in this way. However, one useful feature that has been noticed is that in general 16,000 observations provide about 50% of the spread reduction that is obtained with 128,000 observations, and 16,000 observations is on a steep part of the curve.

It was originally anticipated that there would be some evidence of saturation of observation impact, whereby additional observations produce little additional impact for the high observation numbers. Perhaps surprisingly, this is not the case. However, once the link between EDA spread values and the theoretical error statistics is acknowledged, this result is an obvious consequence of standard data assimilation/retrieval theory.

It is useful to distinguish between having correlated observations and correlated observation errors. Highly correlated observations with uncorrelated errors will always reduce the theoretical analysis/retrieval errors, even if the additional measurements do not effectively add new information to the NWP system. This is simply a result of reducing random measurement noise by repetition, and it is standard experimental practice in a laboratory. Exactly the same arguments apply to the EDA approach. Even though additional measurements might not contain significant new information, they can reduce the spread values of the system by effectively reducing measurement noise through repetition, as long as uncorrelated observation errors are assumed. Therefore, we

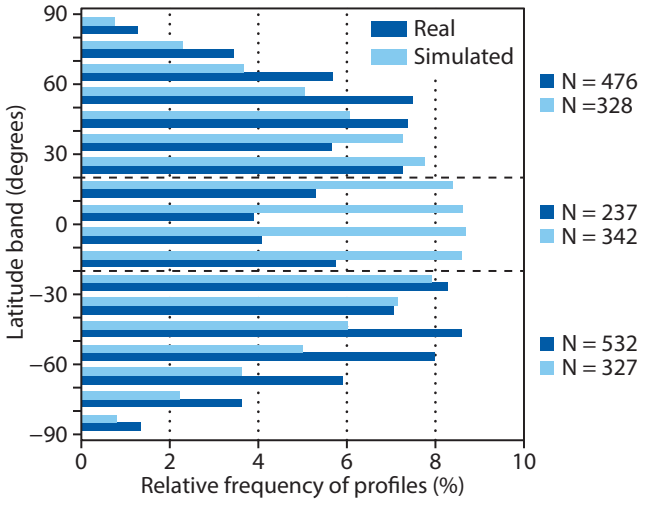

Figure 3 Zonal distribution of real (black) and simulated (grey) GNSS-RO profiles in 10 degree latitude bins for EDA_real (black) and EDA_2 (grey). The relative frequency with respect to the total number of 1245 for EDA_real and 997 for EDA_2 is shown. The horizontal dashed lines separate the southern hemisphere, from the tropics and the northern hemisphere. The bending angle numbers are shown on the right side for real data (black) and simulated data (grey). Results are the average values over the 00 UTC and 12 UTC assimilation cycles in the period 1 July 2008 to 15 August 2008.

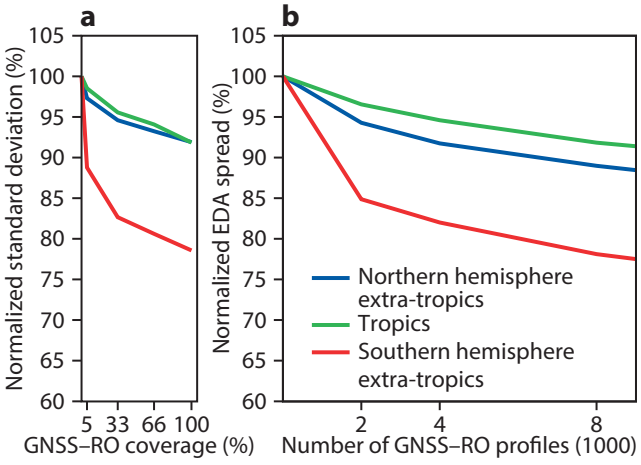

Figure 4 (a) Normalized standard deviation of 24-hour forecast error of observing system experiments as function of the assimilated percentage of real GNSS-RO data and (b) normalized EDA spread (%) at the 24-hour forecast range as function of the assimilated number of simulated GNSS-RO profiles. Results are for temperature at 100 hPa for the period 8 July 2008 to 15 August 2008.

should not expect the curves shown in Figure 5 to plateau and have a zero gradient, until the spread hits a lower limit determined by the assumed model error statistics.

We have investigated if the reduction of the EDA spread at large observation numbers is solely because the additional observations are repetitions of the previous measurements, but this appears not to be the case. An additional EDA experiment was performed using 64,000 observations, but doubling the assumed observation error variances. We found that the 64,000 'degraded' observations produced lower spread values than 32,000 observations with the standard errors.

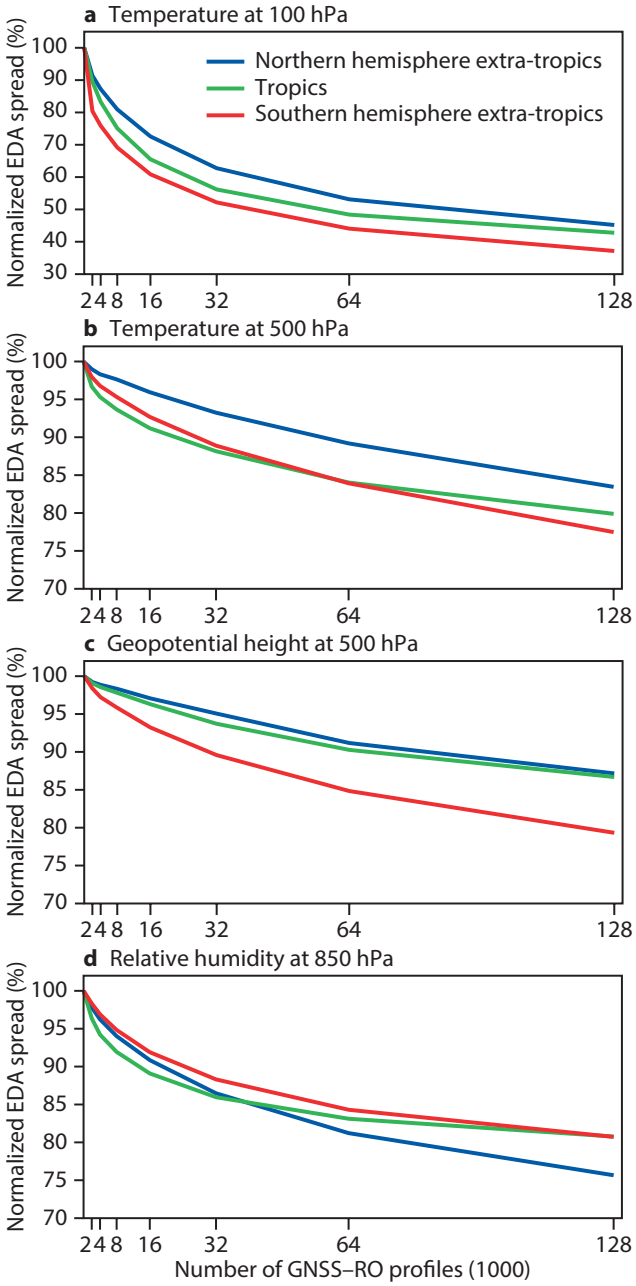

Figure 5 Normalized EDA spread (%) at analysis time as function of the assimilated number of simulated GNSS-RO profiles for (a) temperature at 100 hPa, (b) temperature at 500 hPa, (c) geopotential height at 500 hPa and (d) relative humidity at 850 hPa. Results are for the period 8 July 2008 to 15 August 2008.

EDA spread-skill relationship when using simulated observations

As noted earlier, in standard EDA experiments using real observations, there is a clear relationship between the EDA spread and analysis and short-range forecast error statistics. The EDA spread values will provide useful information about the actual error statistics of the NWP system, provided the assumed observation and model error statistics are reasonable.

This spread-skill relationship breaks down with simulated data because the assumed GNSS-RO observation errors are clearly incorrect. In reality, the simulated observations provide no new information about the atmospheric state because they have been derived from ECMWF analyses. Therefore, it should be noted that the assimilation of the simulated GNSS-RO measurements cannot improve the actual skill of the NWP forecasts, even if the spread values have been reduced (see *Harnisch et al.*, 2013).

Summary and future work

We have used the EDA system to estimate the impact of increasing the number of GNSS-RO measurements from their current levels of ~2,500 per day up to 128,000 profiles per day. We do not reach a saturation of forecast impact, but broadly speaking 16,000 observations per day have around half the impact of 128,000 observations on the EDA spread values. The results suggest that there will be a benefit from increasing the number of the GNSS-RO measurements, and we believe the aim should be to provide at least 16,000 to 20,000 operational measurements per day.

The EDA has proved to be a very useful and efficient tool for this study. In future work, it might be possible to refine the results and look at the impact of different observation sampling patterns. It would also be interesting to compare EDA results with OSSEs for a common period.

FURTHER READING

Andersson, E. & **M. Masutani**, 2010: Collaboration on Observing System Simulation Experiments (Joint OSSE). *ECMWF Newsletter No. 123*, 14–16.

Bauer, P., G. Radnoti, S. Healy & **C. Cardinali**, 2013: GNSS radio occultation constellation observing system experiments. *ECMWF Tech. Memo. No. 692*.

Bonavita, M., L. Isaksen & **E. Hólm**, 2012: On the use of EDA background error variances in the ECMWF 4D-Var. Q. J. *R. Meteorol. Soc.*, **138**, 1540–1559.

Isaksen, L., J. Haseler, R. Buizza & **M. Leutbecher**, 2010: The new Ensemble of Data Assimilations. *ECMWF Newsletter No. 123*, 17–21.

Harnisch, F., S.B. Healy, P. Bauer & **S.J. English**, 2013: Scaling of GNSS radio occultation impact with observation number using an ensemble of data assimilations. *ECMWF Tech. Memo. No. 693*.

Tan, D.G.H., E. Andersson, M. Fisher & **I. Isaksen,** 2007: Observing-system impact assessment using a data assimilation ensemble technique: application to the ADM-Aeolus wind profiling mission. *Q. J. R. Meteorol. Soc.*, **133**, 381–390.

Special Project computer allocations for 2013–2014

The allocations for 2013 have been approved. The figures for 2014 indicate what has been requested.

Member State	Institution	Project title	2013		2014	
			HPCF (units)	Data storage (Gbytes)	HPCF (units)	Data storage (Gbytes)
CONTINUATION PROJECTS						
Austria	University of Vienna (Haimberger)	Homogenization and uncertainty estimation of historic in situ upper air data	10,000	1,000	10,000	1,000
	University of Vienna (Serafin)	Numerical modelling of boundary layer processes over complex terrain	230,000	1,800	X	X
Belgium	RMI (Deckmyn)	Boundary conditions for ALADIN, ALARO and AROME based on IFS, ECMWF EPS and ERA-Interim data	130,000	800	130,000	800
Denmark	DMI (Baklanov)	EnviroChemistry on ECMWF	4,000,000	9,000	4,000,000	9,500
Finland	FMI (Ollinaho)	Model parameter perturbations in ensemble prediction	850,000	8,000	1,250,000	8,000
France	IPSL (Bekki)	Validation and improvement of a stratospheric microphysical aerosol scheme in the IFS	700,000	1,800	700,000	2,400
	Météo-France (Bouttier)	Continental winter weather prediction with the AROME ensemble prediction system	5,000,000	4,000	6,000,000	4,000
	Mercator Ocean (Chanut)	High resolution ocean modelling over Iberian, Biscay and Irish seas	12,000,000	35,000	X	X
	Mercator Ocean (Garric)	The freshwater representation in the Mercator Ocean global ocean reanalysis	12,000,000	20,000	X	X
	IPSL (Lapeyre)	Using Lyapunov covariant modes for atmospheric predictability	10,000	100	10,000	100
	CERFACS (Weaver)	Ensemble variational data assimilation with NEMOVAR	1,000,000	10,000	1,000,000	10,000
Germany	KIT, Karlsruhe) (Anwender)	Impact of blocking and tropical-extratropical interactions on predictability in the Atlantic-European Sector	420,000	4,000	450,000	5,000
	University of Hohenheim (Bauer, Wulfmeyer)	Validation and improvement of high-impact weather process understanding in Europe with the aid of high-resolution WRF simulations and sophisticated data assimilation (VALPUDA)	300,000	3,000	300,000	3,000
	University of Munich (Craig)	Large-scale and local control of severe weather: towards adaptive ensemble forecasting	300,000	500	X	X
	FU Berlin (Cubasch, Kirchner)	Analysis of the coupling between the ocean and atmosphere large scale circulation regimes from annual to decadal time scales	20,000	4,000	20,000	5,000
	DLR (Doernbrack)	Mission support system for HALO research flights	100,000	80	100,000	80
	DLR (Doernbrack)	Source spectra for convectively generated gravity waves - adaptive numerical simulations	200,000	80	200,000	80
	Univ. Cologne (Elbern)	Monitoring Atmospheric Climate and Composition - Interim Implementation (MACC-II)	2,310,000	14,600	2,370,000	14,600
	KIT, Karlsruhe (Gantner, Kalthoff)	Convection-permitting ensemble simulations for West Africa based on different soil moisture fields	350,000	800	200,000	800
	DLR (Gierens)	The impact of fluctuations of temperature, humidity and wind on cirrus clouds	300,000	200	300,000	200
	DLR (Hoinka)	The global circulation in various coordinate systems	500	10	500	10
	AWI, Bremerhaven (Jung)	The global impact of explicitly resolving small-scale processes: A model study with the finite element sea ice-ocean model FESOM	490,000	5,000	490,000	5,000

Germany	FU Berlin (Langematz)	Simulations with an atmosphere-ocean-chemistry-climate Model for the development of a decadal climate prediction system	1,650,000	9,000	760,000	3,000
	FZ Juelich (Stein)	Global atmospheric chemistry modelling	610,000	30,000	610,000	30,000
Italy	ISMAR-CNR (Bertotti)	Effect of rain on the growth and evolution of sea waves	250,000	200	X	X
	IINAF (Masciadri)	Optical turbulence modelling for astronomical applications: towards the Extremely Large Telescopes (ELTs)	1,080,000	300	X	X
	ARPA-SIMC, CNMCA (Montani, Torrisi)	Experimentation of different strategies to generate a limited-area ensemble system over the Mediterranean region	1,200,000	110	1,200,000	120
	CNMCA (Torrisi, Marcucci)	Data assimilation and short-range forecast with a limited area ensemble Kalman filter	3,750,000	1,500	4,500,000	2,000
	ARPA-SIMC, DWD, MeteoSwiss (Montani, Majewski, Steiner)	Implementation of a limited-area ensemble prediction system for Sochi Olympic Games	4,450,000	70	2,000,000	60
	ARPA-SIMC, ISAC-CNR (Pavan, Buzzi)	Multi model monthly ensemble	490,000	100	490,000	100
Ireland	UCD (Sweeney)	Downscaling a wetter/hotter outlier GCM for the EURO-CORDEX initiative	8,000,000	10,000	X	X
Netherlands	KNMI (Attema)	Evaluation of model precipitation for the current climate when using imperfect (GCM) boundaries	499,000	3,000	499,000	3,000
	KNMI (Haarsma)	Decadal predictions	2,400,000	2,000	X	X
	KNMI (Hazeleger)	EC-Earth: developing a European Earth System Model based on ECMWF modelling systems	15,000,000	40,000	15,000,000	40,000
	KNMI (Huijnen)	Inline chemistry for reactive trace gases within IFS	300,000	250	300,000	250
	KNMI (Onvlee)	The Hirlam-B project	4,950,000	15,000	X	X
	KNMI (Selten)	The role of clouds in model bias and climate sensitivity	300,000	2,000	X	X
	KNMI (van den Hurk)	Land use change in the 21st century	500,000	1,000	500,000	1,000
	KNMI (van Noije)	Modelling interactions between atmospheric composition and climate changes with the Earth system model EC-Earth	3,800,000	6,500	3,000,000	5,000
	KNMI (Verkley)	Implementation and validation of radar data-assimilation in the HARMONIE mesoscale weather prediction model	300,000	400	300,000	400
	KNMI (Williams)	Investigation of aerosol feedbacks on decadal timescales	200,000	100	200,000	100
Norway	NILU (Kristiansen)	FLEXPART transport simulations of volcanic ash clouds and gas tracer for the Norwegian community Earth System Model	50,000	150	50,000	150
	University of Oslo (Kristjansson)	Modelling of chemistry-climate interaction	50,000	2,000	50,000	2,000
	DNMI (Frogner)	Hirlam - Aladin Probabilistic Systems	10,000,000	50,000	12,000,000	50,000
Spain	Univ. Illes Balears (Cuxart)	Atmospheric boundary layer processes in complex terrain	150,000	200	150,000	200
	Institut Catala de Ciencies (Doblas- Reyes)	Seasonal climate forecast quality with EC-Earth: role of initialization and stochastic physics	3,960,000	3,300	5,880,000	4,200
Sweden	SMHI (Undén)	European regional re-analysis for monitoring and observations	2,500,000	12,000	X	X
Switzerland	Institute for Atmospheric and Climate Science, ETH Zurich (Boettcher, Joos)	Diabatic effects in mid-latitude weather systems	70,000	3,000	70,000	3,000

United Kingdom	King's College London (Cloke)	IFS water cycle verification using river discharge observations	250,000	6,000	250,000	9,000
	University of Reading (Hodges)	Changes in precipitation extremes associated with extra-tropical Cyclones: System centred dynamical downscaling	500,000	500	500,000	500
	University of Birmingham (Leckebusch)	Investigation of large scale precursor conditions for extreme cyclone development in the extra-tropics	5,000	2,000	5,000	2,000
	Oxford University (Palmer)	Representing uncertainty in weather and climate prediction	5,000,000	6,000	8,000,000	10,000
	Oxford University (Palmer)	Representing uncertainty in ocean observations and the ocean model for extended-range ensemble prediction	5,000,000	6,000	8,000,000	10,000
	Keele University (Shrira)	New kinetic equations and their modelling for wind wave forecasting	100,000	100	100,000	100
	University of Leeds (Woodhouse)	Development and testing of a microphysical aerosol scheme in the IFS forecasting	500,000	5,000	500,000	8,000
JRC	JRC-IES (Bergamaschi)	Global and regional inverse modelling of atmospheric CH4 and N2O	500,000	400	500,000	400
	JRC-IES (Dentener)	Pollution in world regions: analysis of past trends with sensitivity simulations	200,000	470	220,000	490
	JRC (Dosio)	Climate change impacts on the European ecosystems and assessment of forest fires risk	300,000	200	X	X

NEW PROJECTS

Denmark	DMI (Yang)	Last glacial maximum and mid-holocene climate in EC-Earth	495,000	5,000	495,000	5,000
France	Météo-France (Gueremy)	Sensitivity of decadal forecast to atmospheric resolution and physics	11,600,000	40,000	14,500,000	30,000
Germany	AWI, Bremerhaven (Jung)	The role of the polar regions in weather and seasonal prediction	615,000	3,300	2,950,000	12,000
Italy	ISAC (Federico)	A general-purpose data assimilation and forecasting system	150,000	200	150,000	200
	ARPA-SIMC (Marsigli)	Development of a perturbation strategy for convection-permitting ensemble forecasting over Italy	1,500,000	200	1,500,000	200
Netherlands	KNMI (Burgers)	An extreme wind climatology for Dutch water defences	2,000,000	3,000	3,000,000	4,000
	KNMI (Drijfhout)	Implementing and testing an ocean carbon cycle in ECEARTH	480,000	400	480,000	600
Norway	NILU (Orsolini)	SNOWGLACE2 – Impact of snow initialisation on spring sub-seasonal forecasts	1,200,000	1,000	X	X
Sweden	SMHI (Jones)	High resolution regional climate projections at 2°C global warming thresholds	12,000,000	40,000	15,000,000	50,000
ICTP	ICTP (Kucharski)	Interactions between the Atlantic Ocean, African monsoon, the Indian and Pacific Oceans using the EC-Earth and IFS modelling systems	300,000	1,000	300,000	1,000
	ICTP (Tompkins)	Use and value of ECMWF short-range and seasonal forecast products for health impacts in developing countries	300,000	100	300,000	100
Total Requested			**150,224,500**	**436,820**	**121,839,500**	**357,740**

Member State computer allocations for 2013

Member State	HPCF (kunits)	Data Storage (Gbytes)
Austria	55,444	230,356
Belgium	61,729	256,470
Denmark	51,688	214,752
Finland	47,223	196,200
France	203,693	846,298
Germany	251,888	1,046,536
Greece	51,245	212,911
Iceland	31,956	132,772
Ireland	44,589	185,258
Italy	167,158	694,505
Luxembourg	33,663	139,863
Netherlands	82,301	341,941
Norway	56,412	234,381
Portugal	45,699	189,870
Spain	123,729	514,065
Sweden	60,424	251,046
Switzerland	61,061	253,694
Turkey	62,532	259,806
United Kingdom	195,066	810,456
Allocated to Special Projects	**150,224**	**436,820**
Reserved for Special Projects	**37,276**	**152,000**
Total	**1,875,000**	**7,600,000**

TAC and Computing Representatives and Meteorological Contact Points

Member States	TAC Representatives	Computer Representatives	Meteorological Contact Points
Austria	Dr G. Kaindl	Mr M. Langer	Dr A. Schaffhauser
Belgium	Dr D. Gellens	Mrs L. Frappez	Dr J. Nemeghaire
Denmark	Mr C. Simonsen	Mr T. Lorenzen	Mr H. Gisselø
Finland	Mr J. Hyrkkänen	Mr M. Aalto	Mr P. Nurmi
France	Mr J.-M. Carrière	Mr D. Birman	Ms N. Girardot
Germany	Dr D. Schroeder	Dr E. Krenzien	Mr T. Schumann
Greece	Mr A Emmanouil	Mr M Manousakis	Mr A Lalos Ms C Petrou Mr P Skrimizeas Ms T Tzeferi
Iceland	Mr T. Hervarsson	Mr V. Gislason	Mrs K. Hermannsdóttir
Ireland	Ms S. O'Reilly	Mr T. Daly	Mr G. Fleming
Italy	Dr M. Ferri	Mr A. Vocino	Dr T. La Rocca
Luxembourg	Mr J. Santurbano	Mr J. Santurbano	Mr J. Santurbano
Netherlands	Mr R. van Lier	Mr H. de Vries	Mr J. Diepeveen
Norway	Mr E. Martinsen	Ms R. Rudsar	Dr B Røsting
Portugal	Mrs T. Abrantes	Mr B. Anjos	Mr N. M. Moreira
Slovenia	Mr J. Jerman	Mr P. Hitij	Mr B. Gregorčič
Spain	Mr P. del Rio	Mr R. Corredor	Mrs F. Aguado
Sweden	Mr F. Linde	Mr R. Urrutia	Mr F. Linde
Switzerland	Dr P. Steiner	Mr P. Roth	Mr E. Müller
Turkey	Mr M. Fatih Büyükkasabbaşi	Mr F. Kocaman	Mr A. Guser
United Kingdom	Dr A. Dickinson	Mr R. Sharp	Mr I. Forsyth
Co-operating States			
Bulgaria	Ms I. Etropolska	Ms I. Etropolska	Mrs A. Stoycheva
Croatia	Ms B. Matjacic	Mr V. Malović	Mr Č. Branković
Czech Republic	Ms A. Trojakova	Mr K. Ostatnický	Mr F. Sopko
Estonia	Mr T. Kaldma	Mr H. Kaukver	Mrs M. Merilain Mrs T. Paljak
the former Yugoslav Republic of Macedonia	Mr V. Dimitriev	Mr B. Sekirarski	Ms N. Aleksovska
Hungary	Dr Z. Dunkel	Mr I. Ihász	Mr I. Ihász
Israel	Mr I. Rom	Mr V. Meerson	Mr N. Stav
Latvia	Mr A. Bukšs	Mr A. Bukšs	Ms A. Niznika
Lithuania	Mrs V. Auguliene	Mr M. Kazlauskas	Mrs. V. Raliene
Montenegro	Mr A. Marčev	Mr A. Marčev	Ms M. Ivanov
Morocco	Mr H. Haddouch	Mr M. Jidane	Mr K. Lahlal
Romania	Mrs F. Georgescu	Mr R. Cotariu	Ms M. Georgescu
Serbia	Ms L. Dekic	Mr V. Dimitrijević	Mr B. Bijelic
Slovakia	Mr J. Vivoda	Dr O. Španiel	Dr M. Benko
Observers			
EUMETSAT	Mr M. Rattenborg	Dr S. Elliott	
WMO	Mr M. Jarraud		

ECMWF Council and its committees

The following provides some information about the responsibilities of the ECMWF Council and its committees. More detail can be found at:
http://www.ecmwf.int/about/committees

Council

The Council adopts measures to implement the ECMWF Convention; the responsibilities include admission of new members, authorising the Director to negotiate and conclude co-operation agreements, and adopting the annual budget, the scale of financial contributions of the Member States, the Financial Regulations and the Staff Regulations, the long-term strategy and the programme of activities of the Centre.

President Mr François Jacq *(France)*

Vice President Mr Christian Plüss *(Switzerland)*

Policy Advisory Committee (PAC)

The PAC provides the Council with opinions and recommendations on any matters concerning ECMWF policy submitted to it by the Council, especially those arising out of the Four-Year Programme of Activities and the Long-term Strategy.

Chair Mr Juhani Damski *(Finland)*

Vice Chair Mr Arni Snorrason *(Iceland)*

Finance Committee (FC)

The FC provides the Council with opinions and recommendations on all administrative and financial matters submitted to the Council and shall exercise the financial powers delegated to it by the Council.

Chair Mr Detlev Frömming *(Germany)*

Vice Chair Mr Marco Viljanen *(Finland)*

Scientific Advisory Committee (SAC)

The SAC provides the Council with opinions and recommendations on the draft programme of activities of the Centre drawn up by the Director and on any other matters submitted to it by the Council. The 12 members of the SAC are appointed in their personal capacity and are selected from among the scientists of the Member States.

Chair Dr Jan Barkmeijer *(KNMI)*

Vice Chair Prof. Michael Tjernström *(Sweden)*

Technical Advisory Committee (TAC)

The TAC provides the Council with advice on the technical and operational aspects of the Centre including the communications network, computer system, operational activities directly affecting Member States, and technical aspects of the four-year programme of activities.

Chair Dr Daniel Gellens *(Belgium)*

Vice Chair Mr Jean-Marie Carrière *(France)*

Advisory Committee for Data Policy (ACDP)

The ACDP provides the Council with opinions and recommendations on matters concerning ECMWF Data Policy and its implementation.

Chair Mr Klaus Haderlein *(Germany)*

Vice Chair Mr Frank Lantsheer *(Netherlands)*

Advisory Committee of Co-operating States (ACCS)

The ACCS provides the Council with opinions and recommendations on the programme of activities of the Centre, and on any matter submitted to it by the Council.

Chair Mr Milan Dacić *(Serbia)*

Vice Chair Mr Pavol Nejedlík *(Slovakia)*

ECMWF Calendar 2013

Jun 5–7	Using ECMWF's forecast
Jun 12	Joint session of the Technical Advisory Committee and Finance Committee
Jun 19–20	Council (79th Session)
Jun 24–27	ECMWF-WWRP/THORPEX Workshop on 'Polar prediction'
Jul 1–4	CLIVAR GSOP/GODAE Ocean View Workshop on 'Ocean Reanalyses Intercomparison
Jul 1–4	Training Course – ECMWF/EUMETSAT NWP-SAF satellite data assimilation
Sep 2–6	Annual Seminar on 'Recent developments in numerical methods for atmosphere and ocean modelling"
Oct 7–11	Training Course – Use and interpretation of ECMWF products for WMO Members
Oct 14–16	Scientific Advisory Committee (42nd Session)
Oct 17–18	Technical Advisory Committee (45th Session)
Oct 21–22	Finance Committee (93rd Session)
Oct 22–24	Workshop on 'Parameter estimation and inverse modelling for atmospheric composition'
Oct 25	Advisory Committee of Co-operating States (19th Session)
Oct 28	Policy Advisory Committee (36th Session)
Nov 18-20	14th Workshop on 'Meteorological operational systems'
Nov 4–7	EUMETSAT NWP-SAF Workshop on 'Efficient representation of hyperspectral infrared satellite observations'
Nov 12–13	Security Representatives' meeting
Nov 13–15	Computer Representatives' meeting
Dec 4–5	Council (80th Session)

ECMWF publications

(see http://www.ecmwf.int/publications/)

Technical Memoranda

699 **Magnusson, L., A. Thorpe, M. Bonavita, S. Lang, T. McNally & N. Wedi**: Evaluation of forecasts for hurricane Sandy. *April 2013*

698 **Ling, J., C. Zhang & P. Bechtold**: Large-scale distinctions between MJO and non-MJO convective initiation over the tropical Indian Ocean. May 2013

697 **Albergel, C., W. Dorigo, G. Balsamo, J. Muñoz-Sabater, P. de Rosnay, L. Isaksen, L. Brocca, R. de Jeu & W. Wagner**: Monitoring multi-decadal satellite earth observation of soil moisture products through land surface reanalyses. *April 2013*

696 **McNally, T., M. Bonavita & J.-N. Thépaut**: The role of satellite data in the forecasting of hurricane Sandy. *March 2013*

695 **Albergel, C., W. Dorigo, R.H. Reichle, G. Balsamo, P. de Rosnay, J. Muñoz-Sabater, L. Isaksen, R. de Jeu & W. Wagner**: Skill and global trend analysis of soil moisture from reanalyses and microwave remote sensing. *March 2013*

694 **Vitart, F.**: Evolution of ECMWF sub-seasonal forecast skill scores over the past 10 years. *February 2013*

693 **Harnisch, F., S.B. Healy, P. Bauer & S.J. English**: Scaling of GNSS radio occultation impact with observation number using an ensemble of data assimilations. *March 2013*

692 **Bauer, P., G. Radnoti, S. Healy & C. Cardinali**: GNSS radio occultation constellation observing system experiments. February 2013

ESA Contract Report

Contract 21519/08/I-OL (CCN1). **Abdalla, S.**: Global validation of ENVISAT wind, wave and water vapour products from RA-2, MWR, ASAR and MERIS (2011–2012). Final Report. *March 2013*

Index of newsletter articles

This is a selection of articles published in the *ECMWF Newsletter* series during recent years.
Articles are arranged in date order within each subject category.
Articles can be accessed on the ECMWF public website – www.ecmwf.int/publications/newsletter/index.html